Lawrence Berkeley National Laboratory

LBL Publications

Title

Controlling and Optimizing Photoinduced Charge Transfer across Ultrathin Silica Separation Membrane with Embedded Molecular Wires for Artificial Photosynthesis

Permalink

https://escholarship.org/uc/item/38k5t2pz

Journal

ACS Applied Materials & Interfaces, 13(20)

ISSN

1944-8244

Authors

Zhang, Hongna
Weiss, Ian
Rudra, Indranil
et al.

Publication Date

2021-05-26

DOI

10.1021/acsami.1c00735

Peer reviewed

eScholarship.org Powered by the California Digital Library
University of California

Controlling and Optimizing Photo-Induced Charge Transfer across Ultrathin Silica Separation Membrane with Embedded Molecular Wires for Artificial Photosynthesis

Hongna Zhang[1#], Ian Weiss[2#], Indranil Rudra[3], Won Jun Jo[1], Simon Kellner[1], Georgios Katsoukis[1], Elena Galoppini[2], and Heinz Frei[1*]

e-mail: HMFrei@lbl.gov

1 Molecular Biophysics and Integrated Bioimaging Division, Lawrence Berkeley National Laboratory, University of California, Berkeley, CA 94720, USA

2 Department of Chemistry, Rutgers University, Newark, New Jersey 07102, USA

3 Shell India Markets Pvt. Ltd, Mahadeva Kodigehalli, Bangalore 562 149, India

# Authors contributed equally to this work

(*ACS Appl. Mater. Interfaces*, accepted)

Keywords: Ultrathin silica membrane, charge flux, electron transfer, molecular wires, photocurrent measurements, FT-IRRAS spectroscopy, artificial photosynthesis

Abstract

Ultrathin amorphous silica membranes with embedded organic molecular wires (oligo(*p*-phenylenevinylene), 3 aryl units) provide chemical separation of incompatible catalytic environments of CO_2 reduction and H_2O oxidation while maintaining electronic and protonic coupling between them. For an efficient nanoscale artificial photosystem, important performance criteria are high rate and directionality of charge flow. Here, the visible light induced charge flow from anchored Ru bipyridyl light absorber across the silica nanomembrane to Co_3O_4 water oxidation catalyst is quantitatively evaluated by photocurrent measurements. Charge transfer rates increase linearly with wire density, with 5 nm^{-2} identified as optimal target. Accurate measurement of wire and light absorber densities is accomplished by the polarized FT-IRRAS method. Guided by DFT calculations, four wire derivatives featuring electron donating (methoxy) and withdrawing groups (sulfonate, perfluoro-phenyl) with HOMO potentials ranging from 1.48 to 0.64 V vs. NHE were synthesized and photocurrents evaluated. Charge transfer rates increase sharply with increasing driving force for hole transfer from the excited light absorber to the embedded wire, followed by a decrease as the HOMO potential of the wire moves beyond the Co_3O_4 valence band level towards more negative values, pointing to an optimal wire HOMO potential around 1.3 V vs NHE. Comparison with photocurrents of samples without nanomembrane indicates that silica layers with optimized wires are able to approach undiminished electron flux at typical solar intensities. Combined with the established high proton conductivity and small molecule blocking property, the charge transfer measurements demonstrate that oxidation and reduction catalysis can be efficiently integrated on the nanoscale under separation by an ultrathin silica membrane.

1. Introduction

Closing of the light driven cycle of CO_2 reduction by H_2O oxidation on the shortest possible length scale, the nanometer scale, is beginning to get recognized as an important design feature of artificial photosystems because it allows to minimize efficiency-degrading processes. Chief among them are resistance losses caused by ion transport over macroscale distances and buildup of concentration imbalances, and back or cross reactions.[1-4] To avoid the latter, an ultrathin membrane is required for chemically separating the incompatible H_2O oxidation and CO_2 reduction catalysis environments while maintaining electronic and protonic coupling between them. In fact, completing the cycle of water oxidation and generation of primary reduction intermediates on the nanoscale under membrane separation is a key design feature of natural photosynthesis,[5] which is the only existing technology for making chemical compounds at the terawatt level, the scale required for impact on replacing fossil resources. Towards this goal, we are taking an inorganic oxide-based approach for developing core-shell nanotube arrays in which each nanotube constitutes a complete photosystem for vapor phase CO_2 reduction by H_2O under membrane separation (**Figure S1**).[1,2] Arrangement of the nanotubes in the form of square inch sized arrays enables separation of the evolving O_2 and reduced CO_2 products on all length scales from nanometers to square inches and beyond, thereby extending the performance advantage of complete, nanoscale integrated photosystems to the macroscale. Such chemically robust arrays, once equipped with top and bottom covers, constitute systems free of photocatalytically inactive components for deployment over large areas of non-arable land for CO_2 photoreduction by H_2O to fuel at scale.

The inside surface of each Co_3O_4 nanotube provides the catalytic sites for H_2O oxidation. As shown in previous work,[2,6,7] Co_3O_4 nanoparticles are efficient H_2O oxidation catalysts, and the Co_3O_4 is intensely utilized in novel nanoscale photocatalytic systems.[8,9] The amorphous silica shell of 2-3 nm thickness that surrounds the Co oxide nanotube blocks O_2 and other small molecules from crossover, while molecular wires (oligo(*p*-phenylenevinylene)) made of 3 aryl units, abbreviated as PV3) embedded in the silica control charge transfer from light absorbers on the outside of the silica shell to the Co_3O_4 catalyst on the inside.[10-17] Furthermore, stacked Co_3O_4 and SiO_2 nanolayers were shown to transmit protons at rates that exceed by far those needed to keep up with the solar flux at maximum intensity. Hence, the flow of protons generated by H_2O oxidation on the Co_3O_4 surface through the oxide nanowall to the sites of CO_2 reduction on the opposite side does not pose efficiency limitations under artificial photosynthesis conditions.[18]

While motivated by the specific Co_3O_4-SiO_2 core-shell nanotube system described above, maximizing controlled charge transfer through embedded molecular wires for driving a catalyst on the opposite side of an ultrathin silica separation membrane may open up the efficient coupling of incompatible redox catalysis environments of systems of various designs. The task requires optimization of the coupling and energetic alignment of light absorber, wire, and catalyst. Here, we evaluate the rate of visible light induced charge transfer from light absorber through the silica nanolayer to the Co_3O_4 catalyst by monitoring the photocurrent as function of highest occupied molecular orbital (HOMO) energetics of the wire tuned by varying electron withdrawing or donating properties of substituents. In addition, the effects of wire density and light absorber loading are investigated. For the photocurrent measurements, planar samples are employed which enabled detailed structural characterization of the nanolayers by surface sensitive polarized FT-infrared reflection absorption spectroscopy (FT-IRRAS). To attain

adequate photocurrents, sub-monolayer light absorber coverage of planar samples demanded a strong visible light absorber. For this reason, Ru tris-bipyridyl complex was selected, a widely used photostable and electrochemically reversible light absorber with maximum at 450 nm (ε = 14,500 mol L^{-1} cm^{-1})[19] attached to the silica surface via amide linkage to tripodal silyl phenyl anchor (**Figure 1**).

2. Experimental Section

Synthetic Materials and Methods. All chemicals were purchased from Sigma-Aldrich including HPLC grade (99.8%) solvents, which were dried with 3Å molecular sieve (Alfa-Aesar) for three days and stored in a nitrogen glovebox before use, unless noted otherwise. Four hole conducting molecular wires made of three *p*-phenylenevinylene units (1,4-di((*E*)-styryl)benzene, abbreviated PV3) were studied. These were functionalized in *para* position on one end (ring 1) with a COOH or an ethynyl group for Co_3O_4 attachment via a tripodal anchor, and on the opposite end with either a $SO_3^-Cs^+$, a SO_3Et or a OCH_3 substituent in *para* position of ring 3, or C_6F_5 in place of ring 3. These were synthesized as described in the following (see SI for detailed experimental procedures). Abbreviations for wires, numbering of rings, and HOMO energetics are summarized in **Scheme 1**.

The molecular wire with a carboxylic acid group for Co_3O_4 attachment *via* amide linkage on ring 1 to tripodal silyl aniline anchor, and capped with a sulfonate group (A-PV3-SO_3) was prepared following a previously described method.[14] The wires with an ethynyl group for Co_3O_4 attachment *via* click chemistry on ring 1, and capped with a sulfonate ester (E-PV3-SO_3Et), a *p*-

methoxy group (E-PV3-OCH_3) on ring 3, or with a pentafluorophenyl group as ring 3 (E-PV3-F_5), were synthesized as shown in **Scheme 2,** and as described in the SI. Since the click reaction is Cu(I) catalyzed (copper(I) catalyzed azide alkyne cycloaddition (CuAAC)), it forms the 1,4-regioisomer of the 1,2,3-triazole ring. The synthesis of each wire involved a combination of Pd-catalyzed cross coupling and Wittig reactions. Briefly, Sonogashira coupling of diethyl-4-iodobenzylphosphonate (**1**) with TMS- or TIPS-acetylene produced **2** in good yields (TMS = trimethylsilyl, TIPS = triisopropylsilyl). We found that the TIPS group was stable through each step of the synthesis, and therefore preferable as a protecting group. Ring 2 was added by Wittig reaction between **2** and **3**, followed by deprotection of the diethyl acetal. The resulting aldehyde **4** was reacted in a Wittig reaction with a suitably substituted diethyl benzylphosphonate (**5a-c**) to add ring 3 and form E-PV3-SO_3Et, E-PV3-OCH_3 and E- PV3-F_5, respectively (**Scheme 2**).

The light absorber $[Ru(bpy)_2(dcbpy)]Cl_2$ (bpy = 2,2'-bipyridyl, dcbpy = 4,4'-dicarboxyl-2,2'-bipyridyl) was prepared according to literature procedure.[19]

Pt Electrode Fabrication. 2 nm Ti adhesive layer and 100 nm of Pt (99.99%) were consecutively deposited by e-Beam evaporation (Semicore SC600 e-beam evaporator) at $< 2 \times 10^{-6}$ Torr on Si wafers (prime grade p-type, Addison Engineering Inc.) pre-cleaned by standard RCA procedure.

Co_3O_4 Atomic Layer Deposition. Atomic Layer Deposition (ALD) of cobalt oxide was carried out using a Cambridge Nanotech/Ultratech Savannah 100 system equipped with 300 W hollow cathode plasma source (Meaglow, Inc.) featuring a grounding grid above the sample. The process temperature was 40 °C, and bis-(cyclopentadienyl)cobalt(II) (cobaltocene, $CoCp_2$; min 98% from STREM Chemicals, Inc.) was used as a precursor, heated to 80 °C and purged with

200 sccm high purity Ar during pulse. Oxygen flow and chamber pressure were maintained at 60 sccm and 15 mTorr during the deposition process. $CoCp_2$ dose was 5 s long, followed by 5 s of purging. Oxygen plasma half-cycle was 1 s pre-plasma, 5 s plasma (300 W) and 15 s purging. Two hundred such cycles lead to a deposition of 13 $\pm$ 0.8 nm thick Co_3O_4 layer. Structural identification of the ALD layer as Co_3O_4 (spinel) is shown by the characteristic Co-O stretch modes in the FT-IRRAS at 686 and 602 cm^{-1} (**Figure 2(a)** trace (1)).[18] STEM-EDX and AFM characterization of Co_3O_4 ALD layers was reported in previous publications.[11,18] While uniformly covering the Pt surface, the Co_3O_4 ALD layer is constructed of densely packed 3-5 nm crystallites, which implies that the actual surface area onto which wires are attached is somewhat larger than the geometrical area (footprint).[11]

Thickness Measurement. The thickness of ALD oxide films were measured using spectroscopic ellipsometry (Horiba Jobin UVISEL) in the 900-250 nm range at angles varying from 45 to 70° with 5° steps.

Anchoring of 4-(trimethoxysilyl)aniline (TMSA) or 4-(trimethoxysilyl)benzyl azide (TMSBA) on Co_3O_4. 1.5 x 3 cm^2 Si/Pt/Co_3O_4 substrates were cleaned by sonication in isopropanol for 5 min before being placed in a 0.5 mM toluene solution of TMSA (Gelest) or 0.4 mM toluene solution of TMSBA anchor (Gelest). The solution was refluxed for 4 h. After cooling, the substrates were immersed in THF, sonicated for 10 min, and the solvent was switched to water and refluxed for 1 h. As a final step, the substrates were dried with a N_2 stream and immediately utilized for PV3 attachment or kept in a closed vial for further characterization.

Covalent Attachment of PV3. The amide attachment of the COOH-substituted PV3 to the Si/Pt/Co_3O_4 substrate with bound NH_2-substituted anchor (TMSA) was performed as

follows: 1.0 mg (2.0 μmol) of PV3 and 0.8 mg (2.2 μmol) of peptide coupling reagent HATU (*o*-(7-azabenzotriazol-1-yl)-*N,N,N′,N′*-tetramethyluronium-hexafluorphosphate) were sealed in a Schlenk flask and evacuated on the Schlenk line for 2 hours, then *N,N*-dimethyl formamide (1 mL, anhydrous; Sigma Aldrich) was added by syringe. The solution was stirred for 30 minutes until it became bright yellow. The solution was dropped onto the Si/Pt/Co_3O_4/TMSA substrate, which was placed in a desiccator, which was evacuated and refilled with 1 atm of nitrogen. The procedure was repeated 3 times. After 24 h the substrate was rinsed with water and transferred to a flask containing deionized water, sonicated for 5 min, and dried in N_2.

The click (CuAAC) attachment of PV3 to the Si/Pt/Co_3O_4 substrate with bound azido-substituted anchor (TMSBA) was carried out according to literature.[20] Details of the procedure are described in the SI.

SiO_2 Deposition. Silicon dioxide layers were deposited with the above described Savannah 100 Cambridge Nanotech ALD system. SiO_2 deposition was carried out at 40°C with 150 W plasma power using the following cycle: Under a flow of 5 sccm of Ar the chamber exhaust was closed and a 0.05 s pulse of tris(dimethylamino)silane (3DMSA) introduced to the chamber. The chamber was kept sealed for 60 s before purging with 40 sccm of Ar for 30 s followed by a 5 sccm 45 s purge with O_2. At a pressure of 200 mTorr the plasma was ignited for 5 s followed by purging with Ar for 45 s at 5 sccm. Nineteen such cycles lead to a deposition of 3.59 $\pm$ 0.04 nm thick SiO_2 layer, which is the ALD protocol used for all samples presented in this work. Previous studies have shown that PV3 wires are fully encapsulated by SiO_2 for this number of ALD cycles,[16] and initial photocurrent measurements showed maximum current for samples prepared with between 18 and 20 ALD cycles.[21] Structural identification of the ALD

layer as amorphous SiO_2 is confirmed by the characteristic longitudinal optic (LO) SiOSi asymmetric stretch at 1226 cm^{-1} in the FT-IRRAS shown in **Figure 2(a)** trace (1).[14] Cross sectional HR-TEM and AFM images of silica nanolayers deposited by the plasma-enhanced ALD method on Pt reported in a previous paper demonstrate uniformity,[22] while a scanning TEM-EDX image of a SiO_2 ALD layer grown on Co_3O_4 nanolayer shows uniformity as well (Figure 3A of Ref. 7). Conformal property of the SiO_2 layers was shown by O_2 blocking and suppression of redox activity of standard redox couples such as ferrocene or ferrocyanide.[11,15] An atomic Si/O ratio of 0.51 $\pm$ 0.05 for the silica ALD layer was determined by high resolution XPS of an SiO_2 layer deposited on bare Pt (Figure S2 of Ref. 7).

Covalent Attachment of Light Absorber on SiO_2 Surface. For $[Ru(bpy)_2(dcbpy)]^{2+}$ attachment to the silica layer, TMSA was anchored on the SiO_2 surface followed by reaction with a carboxylic group of the dcbpy ligand to form an amide bond using the same method described above for PV3 attachment to anchored silyl aniline.

TiO_2 Deposition. ALD of titanium dioxide was conducted with the same Oxford FlexAl-Plasma Enhanced ALD system. The process temperature is 40 °C, and tetrakis(dimethylamido) titanium(IV) (TDMAT; 99.999% from Sigma Aldrich) and oxygen plasma served as a precursor and an oxidant, respectively. Oxygen gas flow was kept at 60 sccm throughout the deposition process. The titanium precursor exposure half cycle consisted of 2 s dosing and 10 s purging using 250 sccm high purity Ar gas. The oxygen plasma half cycle consisted of 2 s pre-plasma treatment, 3 s plasma exposure, and 5 s purging with 100 sccm N_2 and 250 sccm Ar. Plasma power of 250 W was applied for 3 s during the oxygen plasma half cycle. The deposition chamber pressure was held at 80 mTorr during the TDMAT dosing and purging steps and 15

mTorr during the oxygen plasma steps. Forty-five such cycles lead to a deposition of 5.0 ± 0.07 nm thick TiO_2 layer.

FT-IRRAS Measurements. IRRAS spectra were recorded on a Bruker FT-IR spectrometer model Vertex 80 equipped with a LN_2 cooled HgCdTe detector, a computer controlled reflection accessory Bruker model A513/QA, and wire-grid polarizer model F350. The mirror angle of the IRRAS accessory was fixed at 80° and the grid polarizer switched between p and s polarization, and an aperture of 2.5 mm was used (p refers to perpendicular orientation with respect to both the line of light propagation and the surface, and s refers to parallel to the surface and perpendicular to the line of light propagation). Twenty spectra of 400 scans each at 2 cm^{-1} resolution were recorded and averaged. Sample single beam spectra with p polarization were divided by single beam spectra of reference sample (aluminum mirror) and the negative logarithm calculated. A corresponding absorbance spectrum for the s polarized configuration was computed and subtracted from the p polarized absorbance spectrum

$$-\log_{10}(p, \text{sample}/p, \text{ref}) - [-\log_{10}(s, \text{sample}/s, \text{ref})]$$

From this result, a Pt or Pt/Co_3O_4 background was subtracted. The background absorbance spectrum was determined by the same computational method as used for the sample. All figures show spectra calculated according to this method, unless noted otherwise. Bands of residual atmospheric water vapor in the sample compartment were computationally eliminated as well.

UV-vis Measurement. UV-vis measurements were recorded with a Shimadzu spectrometer model 2450 either in standard transmission mode, or transmission mode using an integrated sphere accessory model ISR-2200. In the latter configuration, scattered transmitted light as well as transmitted light in the direction of the incident probe beam was collected.

Photoelectrochemical Measurements. For photocurrent measurements in 3-electrode configuration at an applied voltage equal to the measured open circuit voltage, the working electrode was illuminated with 476 nm Ar ion laser light (Coherent model Innova-90) (**Figure 1**). The size of the 476 nm laser beam impinging on the working electrode was 0.66 cm^2 and the sample area exposed to the electrolyte solution was 0.42 cm^2. A Pt wire served as counter electrode and Ag/AgCl as reference electrode. Experiments were controlled with a CH Instruments model CH1604E potentiostat.

DFT calculations. Density Functional Theory (DFT) techniques were used for total energy and geometry optimization calculations with tight convergence criteria as implemented in Gaussian 09 software. In all calculations, we used B3LYP exchange correlation functional and 6-31+G** basis set. As widely practiced in DFT literature, Kohn-Sham orbital energetics was used as approximation to HOMO and LUMO energy.

3. Results and Discussion

3.1 Structure and Density of Molecular Wires and Light Absorbers by FT-IRRAS and UV-vis spectroscopy

Molecular wires embedded in ultrathin silica layers were attached to the tripodal silyl aniline or silyl benzyl azide anchors on the Co_3O_4 catalyst surface by an amide or a triazole linkage via 'click' chemistry (specifically, Copper(I)-catalyzed alkyne-azide cycloaddition, CuAAC), respectively. For attachment of the $[Ru(bpy)_2(dcbpy)]^{2+}$ light absorber on the silica membrane surface after encasing the wires in an amorphous SiO_2 layer, amide coupling to the silyl aniline

anchor was used for all samples, with the complete assembly schematically shown in **Figure 1**. While covalently attached to surfaces, the distribution of embedded wires and light absorber molecules is random as there is no molecularly defined linkage between them. The selected loading densities assured that the average distance between anchored Ru complex and wire terminus at the silica surface is less than 1 nm and therefore suitable for charge transfer. This approach serves to explore simple hierarchical assembly methods in order to enable scalability.

3.1.1 Wire and Light Absorber Attached to Tripodal Anchor by Amide Linkage

The detailed FT-IRRAS characterization of the stepwise assembly of Pt/Co_3O_4/TMS-Am-PV3-SO_3/SiO_2 samples, schematically shown in **Figure S2**, was presented in a previous paper.[12] Comparison of polarized FT-IRRAS and non-polarized GATR FT-IR measurements (grazing incidence attenuated total reflection FT-IR) demonstrated the vertical orientation of the wires, which ensures that the embedded molecules span the silica membrane face-to-face. Spectra of the corresponding preparations for the experiments reported here are displayed in **Figure S3** traces (1)-(4).

The $[Ru(bpy)_2(dcbpy)]^{2+}$ light absorber was covalently anchored on the SiO_2 surface by one of the carboxyl groups of the bipyridyl ligand through an amide bond with the NH_2 group of the tripodal TMSA anchor (**Figure 1**). Corresponding IRRAS data before and after linkage of the Ru complex to TMSA anchored on the silica of a Pt/Co_3O_4/SiO_2 sample (no embedded wires) are shown in **Figure 2(a)** trace (2) and trace (3), respectively. The sample before attachment of TMSA showing bands of Co_3O_4 (686, 602 cm^{-1}) and SiO_2 (1226 and 820 cm^{-1})[18] is displayed in trace (1) for reference. In addition to the characteristic bands of TMSA (1621, 1602, 1510, 1416,

1293, 1272, 1193, 1139, 1107(sh), 1060(sh), 524 cm^{-1}) with detailed assignments presented in previous work,[16] **Figure 2(a)** trace (3) shows pronounced amide I (1660 cm^{-1}) and amide II (1520 cm^{-1} (shoulder)) modes of the linkage. Ligand-centered infrared bands of $[Ru(bpy)_2(dcbpy)]^{2+}$ are readily discerned at 1725, 1590(sh), 1464, 1444, 1393, 1320, 782, 764, and 730 cm^{-1} presented on an expanded scale in **Figure 2(b)**, in good agreement with the infrared spectrum of parent $[Ru(bpy)_3]^{2+}$.[23] The 1725 cm^{-1} C=O stretch of a free CO_2H group on the dcbpy ligand[24] indicates that, for the majority of dcbpy ligands, only one carboxyl group forms an amide linkage to a TMSA anchor. No other bands beyond those assigned to the components described above are observed in the infrared spectra of $Pt/Co_3O_4/SiO_2$/TMS-Am-Ru or corresponding samples with SiO_2 embedded A-PV3-SO_3 wires (**Figure S3**, trace (6)), which confirms that the samples are free of impurities.

Surface densities of anchors, molecular wires and light absorbers were determined by combining measurements of UV-vis absorption spectra of a Co_3O_4/TMS-Am-PV3-SO_3/SiO_2/TMS-Am-Ru sample prepared on a quartz support and FT-IRRAS of a sample with identical composition on Pt support (**Figures S4 and S5**), as described in detail in the SI. The approach takes advantage of the 246 nm absorption band of TMSA anchor with its established extinction coefficient, and the superior spectral sensitivity of FT-IRRAS bands of TMSA for accurately determining the fraction of anchors that covalently link to wire or light absorber molecules (A-PV3-SO_3 (360 nm) and $[Ru(bpy)_2(dcbpy)]^{2+}$ (460 nm) peaks are very weak while the intensity of the TMSA band at 246 nm is adequate for density evaluation (**Figure S4**)). According to the analysis, absorbance of 1.84 x 10^{-3} for the 1510 cm^{-1} band of TMSA corresponds to anchor density of 3.0 nm^{-2}. With the TMSA density established by the intensity of

the infrared bands, the fractional absorbance decrease of its 1621 cm^{-1} NH_2 IRRAS mode upon formation of the amide bond to wire molecule or Ru complex allows accurate determination of the density of wires and light absorbers, respectively. Using these FT-IRRAS measurements, densities of embedded wires and light absorbers for all sample preparations were evaluated.

3.1.2 Wire Attached to Tripodal Anchor by Click Chemistry (CuAAC)

For determining the optimum energy level alignment of the silica embedded molecular wire with the light absorber and Co_3O_4 catalyst to achieve maximum electron transfer efficiency, wires with electron donating or withdrawing substituents on the terminal aryl moiety (ring 3) were synthesized. Each wire featured an ethyne (HC ≡ C-) group in para position of ring 1 for attachment to the N_3 group of the TMSBA anchor by click chemistry (**Scheme 1**). The FT-IRRAS of TMSBA anchored on Co_3O_4, shown in **Figure 3** trace (1) and summarized in **Table 1**, features all bands with only small frequency shifts compared to the FT-IR transmission spectrum of TMSBA crystallites in KBr (**Figure S6** trace (2)). Aromatic CH stretch modes are observed at 3066 and 3021 cm^{-1}, and those of the methylene group at 2949 and 2845 cm^{-1}. The $\nu_{as}(N_3)$ at 2100 cm^{-1} of anchored TMSBA is the same as for free azide.[25] Aryl quadrant and semicircle ring phenyl stretch modes at 1600, 1549, 1497 and 1400 cm^{-1} agree well with corresponding TMSBA/ KBr bands, as do the CH_2 bending mode at 1449 cm^{-1} and δ(CCH) at 1181 cm^{-1}. The intense bands at 1129, 1100, and 1021 cm^{-1} are stretch vibrations of the $Si(-O-Co)_3$ tripod, very close to the corresponding $Si(-O-C)_3$ modes of free TMSBA. A striking difference of the infrared spectra of surface anchored and free TMSBA is the relative intensity of the N_3 stretch band at 2100 cm^{-1}. For the anchor on the surface, the absorbance ratio of the N_3 band and the 1600 cm^{-1} aryl stretch

mode is 1:1 (**Figure S6** trace (1)) while the corresponding ratio for free TMSBA is 10:1 (**Figure S6** trace (2)). This difference is due to the fact that the anchored molecule is probed by p-polarized IRRAS while the powder spectrum is recorded by non-polarized infrared light. It indicates that the N_3 stretch of the anchored TMSBA is mainly s-polarized (parallel to the surface) with only a minor p component while for the aryl stretch the p component dominates.[26] We conclude that the aryl ring of the anchor is perpendicular to the surface while the azide group is oriented mainly in horizontal direction. The latter orientation is facilitated by the presence of the CH_2 group linking the aryl and N_3 moieties, and enables vertical orientation of the PV3 molecular axis upon formation of the triazole ring (**Scheme 1**).

The FT-IRRAS recorded following attachment of the E-PV3-SO_3Et wire by click reaction to the TMSA anchor, designated TMSB-Tz-PV3-SO_3Et (Tz for triazole ring) is shown in **Figure 3** trace (2). In the CH stretch region, a new band at 2915 cm^{-1} attributed to the ethyl group is observed along with the CH modes of the anchor. The decrease of the azide mode at 2100 cm^{-1}, shown on an expanded scale in the inset, directly reports the click attachment reaction. Observed infrared band in the region 2000 - 650 cm^{-1} including spectral assignments are presented in **Table 1**. Characteristic bands of the ethyl sulfonate ester substituent of the wire are at 1343 cm^{-1} ($\nu_{as}(SO_2)$), 1188 cm^{-1} ($\nu_{sym}(SO_2)$), 930 cm^{-1} (ν_{as}(S-O-C)), 696 cm^{-1} (ν_{sym}(S-O-C)), and 569 cm^{-1} ($\delta(SO_2)$). Triazole ring modes are found at 1167 cm^{-1} (stretch), 968 cm^{-1} (in-plane bend), and 837 cm^{-1} (out-of-plane bend).[26-29]

Click attachment of E-PV3-F_5 wire to the TMSBA anchor on Co_3O_4 results in the FT-IRRAS shown in **Figure 4** trace (2), quantifiable by the decrease of the azide mode at 2100 cm^{-1} (inset). Spectral assignments of modes in the fingerprint region are presented in **Table 1**. The

signature of the perfluoro phenyl group is manifested by peaks at 1520 and 1491 cm^{-1} (both admixed with aryl stretch), 1002 (shoulder) and 962 cm^{-1} (admixed with triazole in-plane bending mode). This agrees with the typical pattern according to which C-F stretch modes mix with aryl ring modes in a perfluorophenyl group.[30] Triazole ring modes absorb at 1217, 1156 cm^{-1} (stretch) and 668 cm^{-1} (out-of-plane ring bend).

The FT-IRRAS recorded following attachment of the E-PV3-OMe wire by click reaction to the TMSBA anchor, designated TMSB-Tz-PV3-OMe is shown in **Figure 5** trace (2). The intensity of these wire bands is significantly lower than the intensity of the TMSB-Tz-PV3-SO_3Et and TMSB-Tz-PV3-F_5 bands (the wire density for the spectra shown in Figures 3, 4, and 5 is similar as can be seen from the similar decease of the N_3 stretch absorption upon wire attachment). In the CH stretch region, new bands at 2922 cm^{-1} and 2850 cm^{-1} originate from asymmetric and symmetric CH stretch of the methoxy substituent.[31] As shown in **Table 1**, infrared modes below 2000 cm^{-1} involving the methoxy substituent are observed at 1456 cm^{-1} ($\delta_{as}(CH_3)$) and 1253 cm^{-1} (C_{aryl}-O-C),[32,33] while triazole bands are contribute to absorptions at 1173 (ring stretch), 968 (in-plane bend), and 837 cm^{-1} (out-of-plane bend).[27]

For each of these samples, subsequent casting of the anchored wires into SiO_2 by ALD and attachment of $[Ru(bpy)_2(dcbpy)]^{2+}$ light absorber by TMSA anchor was conducted as described in Sect. 3.1.1.

Densities of azide functionalized anchors, triazole-linked wires and amide-linked Ru light absorbers were calculated based on the assumption that the extinction coefficient of the strong characteristic Si-O-Co stretch mode of the aryl-$Si(OCo)_3$ tripod between 1120 and 1140 cm^{-1}, which is common to both the NH_2 (TMSA) and CH_2-N_3 functionalized anchor (TMSBA), is the

same (i.e. independent of whether the anchor features an aniline or benzyl azide moiety). Therefore, the density of anchored TMSBA could readily be determined by the observed absorbance of the TMSBA mode at 1125 cm^{-1}, with a peak absorbance of 9.1 x 10^{-3} representing 3 anchor molecules nm^{-2}, as described in more detail in the SI. The fractional absorbance decrease of the N_3 IRRAS mode of the TMSBA anchor at 2100 cm^{-1} upon formation of triazole linkage to wires was used to determine the density of the embedded wires (shown in **Figures 3, 4,** and **5** as inset of trace (2)). The density of anchored Ru complexes was determined according to the method described in Sect. 3.1.1.

3.2 Efficiency of Charge Transfer across Silica Membrane by Photocurrent Measurement

Pt supported planar Co_3O_4/wire/SiO_2 samples with anchored $[Ru(bpy)_2(dcbpy)]^{2+}$ complexes were utilized as working electrodes for visible light induced current measurements in order quantify charge flow from light absorbers to Co_3O_4 catalyst through the silica membrane, as illustrated by the diagram shown in **Figure 1** (photoelectrochemical cell displayed in **Figure S7**). The $[Ru(bpy)_2(dcbpy)]^{2+}$ complexes excited to the MLCT state (λ_{max} = 460 nm, **Figure 6(c)**) inject hole charges into the embedded wire molecules upon electron transfer to sacrificial electron acceptor $S_2O_8^{2-}$ that results in cathodic photocurrent. **Figure 6(a)** red trace (1) shows a Faradaic photocurrent of 15.5 nA cm^{-2} upon 476 nm illumination (121 mW cm^{-2}), with the circuit held at a potential equal to the measured open circuit potential. By contrast, no Faradaic current is observed for a Pt/Co_3O_4/SiO_2/TMS-Am-Ru sample (no embedded molecular wires), only capacitive photocurrent due to the buildup of Ru^{III} on the silica surface (**Figure 6(a)** black trace (2)). It should be added that excitation of Co_3O_4, which absorbs throughout the visible region

(**Figure S4**), does not induce photocurrent as demonstrated in previous work when illuminating a Pt/Co_3O_4 sample (no SiO_2 coating) in the absence of $[Ru(bpy)_3]^{2+}$ sensitizer.[11] We conclude that short circuit photocurrent flows exclusively through embedded molecular wires. The effect of silica embedded wires can be demonstrated with much higher sensitivity when using the orders of magnitude higher concentration of dissolved (non-surface bound) $[Ru(bpy)_3]^{2+}$ light absorber, as shown in **Figure S8(a)**. Samples with or without embedded wires are free of pinholes as confirmed by the absence of waves during CV sweeps using established redox couples (**Figure S8(b)**).

In addition to Faradaic photocurrents, samples with or without embedded wires exhibit capacitive photocurrents manifested by the sharp signal upon illumination onset. For the sample with embedded wires (**Figure 6(a)** trace (1)), an anodic capacitive photocurrent spike is observed. By contrast, cathodic capacitive charging is encountered upon photo-excitation of a sample that lacks embedded wires (**Figure 6(a)** trace (2)). For the sample with embedded wires, the most plausible origin of the capacitive photocurrent is that the replacement of SO_4^{2-}, produced upon electron transfer from excited surface anchored $[Ru(bpy)_2(dcbpy)]^{2+}$ to $S_2O_8^{2-}$, proceeds at slower rate than the rate of photoexcitation of a given Ru complex (see further discussion below). As a result, a repeatedly excited Ru complex can transfer hole charge to embedded wires but is blocked from electron transfer to $S_2O_8^{2-}$ thereby remaining in reduced state until fresh $S_2O_8^{2-}$ diffuses sufficiently close for electron transfer to proceed. Hence, the silica surface on the working electrode is negatively polarized by the buildup of reduced $[Ru^{I}(bpy)_2(dcbpy)]^{+}$. For samples without embedded wires, electron transfer from excited Ru light absorber to $S_2O_8^{2-}$ is not accompanied by hole donation to wires, thus building up oxidized

$[Ru^{III}(bpy)_2(dcbpy)]^{3+}$ that renders the silica surface positively polarized. The opposite sign of the observed capacitive photocurrents for the two types of samples, despite the fact that both processes are cathodic, is attributed to the build-up of opposite charge on the silica surface of the working electrode.

Strong support for attributing the observed low photocurrent to slow replacement of consumed $S_2O_8^{2-}$ acceptor at the silica/electrolyte interface was obtained by photocurrent measurements of samples for which the anchored $[Ru(bpy)_2(dcbpy)]^{2+}$ was encapsulated in a 5 nm thick TiO_2 layer deposited by ALD. It is well established that anchored Ru bipyridyl complexes transfer electrons very efficiently to the TiO_2 conduction band on the ultrafast time scale.[34] Therefore, by inserting a TiO_2 nanolayer between the Ru light absorber and the persulfate electrolyte, the efficient non-radiative decay of the excited $[Ru(bpy)_2(dcbpy)]^{2+}$ MLCT state (decay time 210 ns)[35] that competes with electron transfer to $S_2O_8^{2-}$ is replaced by the less efficient back transfer of TiO_2 conduction band electrons to the oxidized Ru^{3+} center (multiphasic decay of tens to hundreds of μs).[36,37] For the Co_3O_4/TMS-Am-PV3-SO_3/SiO_2/TMS-Am-Ru/TiO_2 sample, the photocurrent after start of 476 nm illumination at 216 mW cm^{-2} was 615 nA cm^{-2}, exceeding the initial photocurrent of a Co_3O_4/TMS-Am-PV3-SO_3/SiO_2/TMS-Am-Ru sample (no TiO_2 layer) of similar wire density by a factor of 21 (normalized for 476 nm laser intensity). We conclude that visible light-driven charge flux through the silica membrane via embedded wires by illumination of anchored light absorbers is limited by the efficiency of electron transfer from the excited Ru complex to the acceptor in the electrolyte solution, which is much higher for the case of the TiO_2 conduction band. Furthermore, when increasing the laser intensity from 216 mW cm^{-2} to 2,580 mW cm^{-2} (factor of 11.9), the current density increased by a factor of 10.4 to

6.370 μA cm^{-2}, as shown in **Figure 6(b)**, demonstrating that there is no indication that silica embedded wires limit photo-induced charge flux in the ten μA cm^{-2} regime. Note the expected decrease to a steady state photocurrent of 1.2 μA cm^{-2} after several seconds due to depletion of $S_2O_8^{2-}$ acceptor ions at the TiO_2/electrolyte interface upon continued photolysis.

To demonstrate that the Ru complex is the sole light absorber responsible for the observed photocurrent, the wavelength dependence of the photocurrent was recorded. As shown in **Figure 6(c)**, the photocurrent at constant laser intensity (92 mW cm^{-2}) at 514, 502, 476, and 458 nm follows the optical absorption profile of the $[Ru(bpy)_2(dcbpy)]^{2+}$ MLCT band.[24,35,38] No contribution to the photocurrent by absorption of light by Co_3O_4 (**Figure S4** trace (6)) is observed.

Comparing photocurrent measurements of Co_3O_4/TMS-Am-PV3-SO_3/SiO_2/TMS-Am-Ru samples with preparations that feature Ru light absorber directly anchored on the Co_3O_4 surface (no silica membrane) provides insight into the efficiency of photoinduced charge flux across the silica membrane. In **Figure 6(d)**, the observed photocurrent of a Pt/Co_3O_4/TMS-Am-Ru sample without silica membrane (red trace (1), 5.8 Ru nm^{-2}) is 47.4 nA cm^{-2} compared to 28.8 nA cm^{-2} for a Co_3O_4/TMS-Am-PV3-SO_3/SiO_2/TMS-Am-Ru sample with membrane (black trace (2), 6.0 PV3-SO_3 nm^{-2}, 8.8 Ru nm^{-2}). The density calculations were based on FT-IRRAS shown in **Figure S9**. The photocurrent of the sample with membrane is 60% of the photocurrent measured for the sample without membrane. We conclude that for a silica membrane with embedded A-PV3-SO_3 wires, the photocurrent amounts to a large fraction of what is observed in the absence of a membrane. With the assumption that the fraction of excited $[Ru(bpy)_2(dcbpy)]^{2+}$ that undergoes electron transfer to $S_2O_8^{2-}$ is the same for the photocurrent measurements with and

without membrane because the non-radiative decay processes of excited $[Ru(bpy)_2(dcbpy)]^{2+}$ that compete with electron transfer to $S_2O_8^{2-}$ are the same for both samples,[39] the result indicates that the electron transfer efficiency from light absorber to Co_3O_4 catalyst through the silica membrane is already about half of the efficiency in the absence of the membrane. As described in the following, optimization of the wire density and wire energetics will allow us to sufficiently improve the efficiency to approach photocurrent levels obtained without membrane.

3.3 Influence of Wire and Light Absorber Density on Photocurrent Efficiency

To optimize the charge transfer across the silica separation membrane, several parameters were varied, starting with the density of molecular wires. Photocurrents were measured for 3 samples with different A-PV3-SO_3 wire density under identical illumination and electrolyte conditions. Observed initial photocurrents after light-on are (1) 27.4 nA cm^{-2} for 4.1 PV3 nm^{-2} (2.8 Ru nm^{-2}), (2) 16.2 nA cm^{-2} for 2.1 PV3 nm^{-2} (1.0 Ru nm^{-2}), and (3) 3.3 nA cm^{-2} for 0.6 PV3 nm^{-2} (3.7 Ru nm^{-2}), as shown in **Figure 7(A)**. The photocurrent is found to increase linearly with wire density (**Figure 7(B)**). For wire density substantially higher than 5 PV3 per nm^{-2}, lack of sufficient SiO_2 ALD deposit in the spaces between wires may begin to adversely affect the integrity of the silica membrane for blocking O_2 and other small molecules.[40] Therefore, 5 nm^{-2} is an optimal target for wire density.

In contrast to the distinct wire density dependence of the photocurrent, there is far less sensitivity of the photocurrent with respect to the density of $[Ru(bpy)_2(dcbpy)]^{2+}$, as manifested by the absence of photocurrent change, within uncertainty, for SiO_2-embedded E-PV3-F_5 samples with up to 9-fold different TMS-Am-Ru density (**Figure S10**). The linear wire density

dependence of the photocurrent, despite the up to factor of 3 different TMS-Am-Ru density, similarly demonstrates the absence of a significant influence of the anchored light absorber density on the photocurrent.

3.4 Influence of Wire Energetics on Photocurrent Efficiency

Equally important for optimizing the electron transfer efficiency is the energy level alignment of light absorber, wire, and Co_3O_4 catalyst. Specifically, the proper potential of the HOMO of the embedded wire is critical for efficient hole charge transfer across the silica membrane. Photocurrents were evaluated for three wire molecules modified on ring 3 as described in Sect. 3.1.2 (**Scheme 1**), namely *p*-ethyl sulfonate in E-PV3-SO_3Et (for comparison with amide linked A-PV3-SO_3), *p*-methoxy in E-PV3-OMe (electron donating), and perfluorophenyl as ring 3 in E-PV3-F_5 (electron withdrawing). Interpretation of the results was based on DFT derived HOMO potentials of the wires. The comparison is rendered feasible by the fact that all wires are attached to the Co_3O_4 surface by the same triazole linkage and use the same anchor moiety (TMSBA). The additional CH_2 group on the anchor, present for synthetic reasons, does not influence the HOMO and LUMO distribution of the wire, as explained in **Figure S11**. Comparison of photocurrent data of *p*-sulfonate wires with triazole and amide linkage, whose HOMO differ by 0.32 V, provided additional insight.

For click attached E-PV3-SO_3Et, photocurrent is shown in **Figure 8(a)** trace (1), together with FT-IRRAS data shown in **Figure 8(b)** for determining the Ru light absorber density. Absorbance of 2.88 x 10^{-3} for the 1125 cm^{-1} band of anchored TMSBA corresponds to a density of 0.95 TMSBA nm^{-2}, while the fractional decrease of the 2099 cm^{-1} azide band upon click attachment of E-PV3-SO_3Et via a triazole ring indicates wire density of 0.72 nm^{-2} (**Figure 3**).

$[Ru(bpy)_2(dcbpy)]^{2+}$ density is calculated as 3.6 nm^{-2} based on the observed TMSA density of 5.4 nm^{-2} and fractional decrease of the NH_2 band (1621 cm^{-1}) of 60% (**Figure 8(b)**). The photocurrent is 39.0 nA cm^{-2} after onset of illumination (**Figure 8(a)** trace (1)). Normalized for the same wire density of 0.6 nm^{-2} as the A-PV3-SO_3 sample (**Figure 7**), the initial photocurrent (33.4 nA cm^{-2}) for E-PV3-SO_3Et is 10 times higher than the 3.3 nA cm^{-2} measured for amide attached A-PV3-SO_3 wire. The large difference is attributed to the 0.32 V stronger driving force for charge transfer from Ru light absorber to click-attached wire HOMO; at the interface with Co_3O_4, isoenergetic occupied Co_3O_4 levels are available for both wires (**Figure 9**).

A distinct feature of the photocurrent of the TMSB-Tz-PV3-SO_3Et sample shown in **Figure 8(a)**, trace (1), is the decay of the Faradaic current, which vanishes after a few seconds under illumination. The photocurrent behavior indicates a decrease of the $S_2O_8^{2-}$ acceptor concentration in the vicinity of the silica surface and the anchored Ru complexes. The effect is attributed to the closeness of the HOMO potential of TMSB-Tz-PV3-SO_3Et and the Co_3O_4 valence band maximum, which results in partial hole population on the embedded wires; any hole population on the wires results in efficient charge recombination with excited $[Ru(bpy)_2(dcbpy)]^{2+}$ electrons, thereby preventing collection of photogenerated holes at the Pt electrode. As the $S_2O_8^{2-}$ concentration in the vicinity of the silica surface decreases, the reduced $[Ru^{I}(bpy)_2(dcbpy)]^{1+}$ density increases, which results in more efficient recombination with holes transferred to embedded wires, diminishing the photocurrent. Application of a cathodic potential moves the Co_3O_4 valence band maximum to more negative values, which decreases the partial hole population on the embedded wires and, hence, reduces the charge recombination process (**Figure 8(a)** trace (2) and trace (3)).

Samples with embedded perfluorophenyl derivatized wires gave a photocurrent of 28.8 nA cm^{-2} upon start of illumination, as shown in **Figure 10(a).** From absorbance of 7.41 x 10^{-3} for the SiOCo mode at 1129 cm^{-1}, a density of 2.44 TMSBA nm^{-2} is calculated. According to the decrease of the 2100 cm^{-1} azido stretch by 60% upon click reaction, a wire density of 1.46 E-PV3-F_5 nm^{-2} is obtained. $[Ru(bpy)_2(dcbpy)]^{2+}$ density is 6.5 nm^{-2} calculated based on the observed TMSA density of 14.2 nm^{-2} and fractional decrease of the NH_2 band (1621 cm^{-1}) of 46% (**Figure S12(a)**). The observed photocurrent density is 28.3 nA cm^{-2}, or 11.6 nA cm^{-2} when normalized for 0.6 nm^{-2} wire density, indicating a factor of 3.5 increase of charge transfer efficiency relative to A-PV3-SO_3 for a driving force increase of hole transfer from Ru light absorber to embedded wire by 0.25 V (**Figure 9**). As can be seen in **Figure 10(a)** the Faradaic photocurrent decreases significantly within a few seconds after onset of illumination indicating partial hole population on the embedded wires due to the closeness of the E-PV3-F_5 HOMO potential and the Co_3O_4 valence band potential. As in the case of click-attached E-PV3-SO_3Et, applying a negative potential of a couple hundred mV suppresses the photocurrent decay.

For click-attached E-PV3-OMe, measurement of the short circuit photocurrent (**Figure 10(a)**) shows no Faradaic cathodic photocurrent at any of the Ru densities used (from 1 to 10 nm^{-2}). FT-IRRAS data for determining wire and Ru light absorber density are presented in **Figure 5 and Figure S12(b)**, respectively. Absorbance of 3.87 x 10^{-3} for the 1129 cm^{-1} band of anchored TMSBA corresponds to a density of 1.27 TMSBA nm^{-2}, while the fractional decrease of the 2099 cm^{-1} azide band upon click attachment of E-PV3-OMe of 38% indicates wire density of 0.5 nm^{-2}. $[Ru(bpy)_2(dcbpy)]^{2+}$ density is 1.2 nm^{-2} calculated based on the observed TMSA density of 3.26 nm^{-2} and fractional decrease of the NH_2 band (1621 cm^{-1}) of 37%. When comparing with the

observed photocurrent for click attached E-PV3-SO_3Et of similar wire density and considering an uncertainty of $\pm$ 1.5 nA, it is found to decrease by over a factor of 20 from E-PV3-SO_3Et to E-PV3-OMe samples. Because the driving force of hole charge transfer from Ru to wire HOMO increases by 0.52 V from sulfonate to methoxy substituted wire and, therefore, expected to result in strongly enhanced rather than reduced photocurrent, the observed opposite trend is attributed to the fact that the HOMO is aligned with the Co_3O_4 bandgap, and hole transfer from E-PV3-OMe to Co_3O_4 is blocked (**Figure 9**).

The photocurrent dependence on wire HOMO potential is summarized in the form of a plot shown in **Figure 10(b)**. It should be added that the large (1.5 cm x 3 cm) planar single layer sample geometry, selected for this work to enable FT-IRRAS characterization of anchored wires and light absorbers for each sample used for photocurrent measurements, proved ideal for quantifying and optimizing loading density and energy level alignment for maximum charge flux through membrane via embedded wires. However, the strong kinetic bottleneck for electron transfer from Ru complex to the acceptor, aggravated by this geometry, renders optimization of the efficiency of light absorber-wire coupling and quantum yield determinations challenging.

3.5 Insights from Wire Density and Energetics Dependence of Photocurrents

The observed dependence of the photo-induced charge flow on density and energetics of the embedded molecular wires revealed by the photocurrent measurements provides a rational path for optimizing the charge transfer efficiency of the ultrathin silica membrane and at the same time reveals key mechanistic insights.

The linear dependence of the photocurrent on embedded wire density (**Figure 7(B)**) indicates that the wires pose a charge transfer bottleneck at low wire density. The 8-fold increase of the photocurrent upon increase of the wire density from 0.6 to 4.1 nm^{-2} is in agreement with the stronger electronic coupling and the reduced reorganization energy that results from shortened average spatial separation of anchored light absorber and ring 3 of an embedded wire molecule.[41] The upper limit for wire density is determined by the functional integrity of the silica nanomembrane in terms of chemical separation and proton conductivity property, with 5 nm^{-2} as a safe target.

By contrast, no substantial dependence of the photocurrent on the anchored light absorber density is observed, as described in Sect. 3.3. The insufficient replenishment of $S_2O_8^{2-}$ acceptor near the silica surface that results in the buildup of reduced $[Ru^{I}(bpy)_2(dcbpy)]^{1+}$ complexes suggests a plausible explanation: At 100 mW cm^{-2} photolysis intensity, the average time interval between arriving photons at a given Ru site is 50 ms. Hole transfer from light absorber via silica embedded wire to Co_3O_4 is an ultrafast process (255 ps) according to our recent transient optical absorption study.[12] Replenishment of $S_2O_8^{2-}$ in electron transfer distance of the Ru complex may be substantially slower, resulting in the observed buildup of reduced $[Ru^{I}(bpy)_2(dcbpy)]^{1+}$ complexes. This steady state buildup of reduced Ru complexes grows larger with increasing light absorber density, resulting in increasingly efficient charge recombination with holes injected into the embedded wires thereby suppressing contribution to Faradaic photocurrent.

The drastic reduction of the kinetic bottleneck for the photo-induced charge flux through embedded molecular wires by introducing a TiO_2 ALD layer as electron acceptor, resulting in observed photocurrents in the ten μA cm^{-2} regime, indicates that silica membranes with

embedded wires are suitable for use in high surface area nanostructured artificial photosystems for operation at maximum solar intensity.

The photocurrent behavior as function of the driving force of hole transfer from excited $[Ru(bpy)_2(dcbpy)]^{2+}$ to embedded wire, displayed in **Figure 10(b)**, demonstrates the high sensitivity of the charge flux with respect to the energy level alignment of light absorber, embedded wire, and catalyst. According to Marcus theory, the kinetics for charge transfer from excited light absorber to embedded wire (Step 1, Figure 9), and from wire to Co_3O_4 (Step 2) is governed by the free energy change, the reorganization energy, and the electronic coupling.[40] For charge transfer from excited $[Ru(bpy)_2(dcbpy)]^{2+}$ to embedded wire molecule, the free energy change is estimated as the difference between the HOMO potential of the wire linked to anchor and the redox potential of the light absorber. While the correction for the silica environment is not available (Weller equation),[8] its influence on the relative rates when comparing the various embedded wires cancels out because all wires are embedded in the same silica medium.

When comparing the photocurrent results of samples with different modified triazole-linked wires but equal wire density, the charge flux dependence is most likely dominated by the free energy change because the reorganization energy and electronic coupling can be assumed to be very similar since no significant variation in the distance between the bipyridyl ligands of anchored $[Ru(bpy)_2(dcbpy)]^{2+}$ and ring 3 of the embedded wire molecule ($-C_6F_5$, $-C_6H_5SO_3Et$, or $-C_6H_5OMe$) is expected. Because the wire molecules are attached to the Co_3O_4 surface by identical TMSBA anchors, reorganization energy and electronic coupling are not expected to be significantly different for charge transfer Step 2, either. Therefore, the observed photocurrents for

the three triazole attached wires indicate a strong dependence of the charge flux on the driving force of the two sequential transfer steps. The 2.9-fold increase of the photocurrent when replacing TMSB-Tz-PV3-F_5 (HOMO + 1.23 V) by TMSB-Tz-PV3-SO_3Et (HOMO + 1.16 V) is mainly attributed to the 70 mV increased driving force of charge transfer from excited $[Ru(bpy)_2(dcbpy)]^{2+}$ to the embedded wire. The influence of the energy level alignment of the embedded wire and Co_3O_4 on the photocurrent is most drastically seen for TMSB-Tz-PV3-OMe (HOMO +0.64 V), which falls within the bandgap of Co_3O_4. We conclude that the observed photocurrent behavior of the click-attached wires is predominantly determined by the driving force of the interfacial charge transfer steps, with embedded wires featuring a HOMO potential around +1.3 V offering rates similar to those observed in the absence of a membrane. The prevailing role of the driving force is consistent as well with the 3.5-fold increase of the photocurrent from TMS-Am-PV3-SO_3 to TMSB-Tz-PV3-SO_3Et as it increases by 0.32 V, although the different chemical linkage to tripodal anchor may involve significant geometrical differences affecting electronic coupling and/or reorganization energy.

Our modular synthetic approach for assembling silica-embedded wire molecules offers additional avenues for further efficiency improvements of charge transport across the ultrathin membrane. While oligo(*p*-phenylenevinylene) structures are shown to be well suited as embedded wire molecules, recent new insights into the role of anchor or linker electronic properties for facilitating rates and control of charge transfer between molecular components and oxide surfaces offer rich opportunities.[42-47] For example, the intramolecular electric dipole moment of a linker manipulated by electron donating or accepting substituents will allow fine-tuning of wire HOMO and LUMO potential, both magnitude and direction.[43-46] Furthermore, the dipole of the triazole linker can be manipulated by appropriate selection of the tautomeric form.[47]

Yet another avenue to explore for tuning the energy level alignment of wire, light absorber and Co_3O_4 is replacing unsaturated TMS aryl anchors by saturated $(-O-CH_2-)_3C$ 'spider' anchors.[10] These opportunities illustrate the power of using molecular design for controlling charge transport across the inorganic oxide membrane.

4. Conclusions

The quantitative evaluation of the photocurrent across an ultrathin silica membrane with embedded molecular wires, combined with FT-IRRAS characterization of light absorber and wire density, allowed the systematic optimization of visible light-induced charge transfer through the membrane. Wires of type oligo(*p*-phenylenevinylene) with 3 aryl units modified on the terminal aryl moiety by a substituent that adjusts the HOMO around + 1.3 V vs. NHE are found to provide optimal energy level alignment with $[Ru(bpy)_2(dcbpy)]^{2+}$ light absorber and Co_3O_4 catalyst. Photocurrents increase linearly with embedded wire density, with 5 nm^{-2} as optimal target. A comparison of photocurrents with and without silica membrane indicates that samples with membrane reach 60% of the charge flux in the absence of a membrane for un-optimized wires (HOMO +1.48 V); observed photocurrent performance upon optimization of wire energetics and density indicates that charge flux values approaching those obtained in the absence of a membrane are achievable.

With high proton conductivity and complete chemical separation of O_2 (and other small molecules) established in previous work for silica layers as thin as 3 nm,[18] the precisely controlled charge transfer property demonstrated here introduces silica nanolayers with embedded wires as an ultrathin membrane for enabling integration of the incompatible

environments such as H_2O oxidation and CO_2 reduction half reactions in a complete nanoscale artificial photosynthetic unit. More generally, inert oxide nanolayers with embedded molecular wires offer a conducting solid interface with unprecedented control for fine-tuning of charge transfer. The wealth of possibilities of using substituents for selecting HOMO and LUMO potentials of organic molecules allows energy level matching of charge transport for improving rates and imposing directionality with unrivaled precision compared to other materials choices. Moreover, the ability to independently optimize charge transport, proton transport, and chemical separation properties by the choice of wires and inorganic solid material for encapsulation is a unique feature for developing efficient functional interfaces of multi-component photocatalytic systems.

Supporting Information

Graphics of systems design and molecular structures; FT-IRRAS and UV-vis of assembly; determination of wire and light absorber density; photocurrent and CV measurements; graphical representation of DFT results; details of wire synthesis, click reaction, NMR characterization.

Acknowledgment

Funding to support this work was provided by the Energy & Biosciences Institute through the EBI-Shell program. Portions of this work (plasma enhanced atomic layer deposition, ellipsometry, e-beam evaporation) were performed as a User Project at The Molecular Foundry, Lawrence Berkeley National Laboratory, which is supported by the Office of Science, Office of Basic Energy Sciences, of the U.S. Department of Energy under Contract No. DE-AC02-05CH11231. E.G. is supported by the U.S. Department of Energy, Office of Science, Office of

Basic Energy Sciences, under Award Number DE-FG02-01ER15256. I.R. would like to thank Flavia Cassiola, Shauvik De and Albert Harvey for stimulating discussions during the course of this work. S. K. acknowledges financial support by a MINT fellowship of the Hanns-Seidel-Stiftung.

References

[1] Edri, E.; Aloni, S.; Frei, H. Fabrication of Core-Shell Nanotube Array for Artificial Photosynthesis Featuring an Ultrathin Composite Separation Membrane. *ACS Nano* **2018**, *12*, 533-541.

[2] Kim, W.; Edri, E.; Frei, H. Hierarchical Inorganic Assemblies for Artificial Photosynthesis. *Acc. Chem. Res.* **2016**, *49*, 1634-1645.

[3] Chabi, S.; Papadantonakis, K. M.; Lewis, N. S.; Freund, M. S. Membranes for Artificial Photosynthesis. *Energy Environ. Sci.* **2017**, *10*, 1329-1338.

[4] Goto, Y.; Hisatomi, T.; Wang, Q.; Higashi, T.; Ishikiriyama, K.; Maeda, T.; Sakata, Y.; Okunaka, S.; Tokudome, H.; Katayama, M.; Akiyama, S.; Nishiyama, H.; Inoue, Y.; Takewaki T.; Setoyama, T.; Minegishi, T.; Takata, T.; Yamada, T.; Domen, K. A Particulate Photocatalyst Water-Splitting Panel for Large-Scale Solar Hydrogen Generation. *Joule* **2018**, *2*, 509-520.

[5] Campbell, N. A.; Reece, J. B.; Taylor, M. R.; Simon, E. J. *Biology: Concepts & Connections,* 5th ed.; Educational Pearson: New York, 2006.

[6] Jiao, F.; Frei, H. Nanostructured Cobalt Oxide Clusters in Mesoporous Silica as Efficient Oxygen-Evolving Catalysts. *Angew. Chem. Int. Ed.* **2009**, *48*, 1841-1844.

[7] Zhang, M.; de Respins, M.; Frei, H. Time-Resolved Observation of Water Oxidation Intermediates on Cobalt Oxide Nanoparticle Catalyst in Aqueous Solution. *Nature Chem.* **2014**, *6*, 362-367.

[8] Zhang, Y.; Jin, Z.; Yuan, H.; Wang, G.; Ma, B. Well-Regulated Nickel Nanoparticles Functional Modified ZIF-67 (Co) Derived Co_3O_4/CdS p-n Heterojunction for Efficient Hydrogen Evolution. *Appl. Surf. Sci.* **2018**, *462*, 213-225.

[9] Yang, H.; Jin, Z.; Liu, D.; Fan, K.; Wang, G. Visible Light Harvesting and Spatial Charge Separation over the Creative Ni/CdS/Co_3O_4 Photocatalyst. *J. Phys. Chem. C* **2018**, *122*, 10430-10441.

[10] Agiral, A.; Soo, H. S.; Frei, H. Visible Light Induced Hole Transport from Sensitizer to Co_3O_4 Water Oxidation Catalyst across Nanoscale Silica Barrier with Embedded Molecular Wires. *Chem. Mater.* **2013**, *25*, 2264-2273.

[11] Edri, E.; Frei, H. Charge Transport through Organic Molecular Wires Embedded in Ultrathin Insulating Inorganic Layer. *J. Phys. Chem. C* **2015**, *119*, 28326-28334.

[12] Edri, E.; Cooper, J. K.; Sharp, I. D.; Guldi, D.; Frei, H. Ultrafast Charge Transfer between Light Absorber and Co_3O_4 Water Oxidation Catalyst across Molecular Wires Embedded in Silica Membrane. *J. Am. Chem. Soc.* **2017**, *139*, 5458-5466.

[13] Frei, H. Photocatalytic Fuel Production. *Curr. Opin. Electrochem.* **2017**, *2*, 128-135.

[14] Katsoukis, G.; Frei, H. Heterobinuclear Light Absorber Coupled to Molecular Wire for Charge Transport across Ultrathin Silica Membrane for Artificial Photosynthesis. *ACS Appl. Mater. Interfaces* **2018**, *10*, 31422-31432.

[15] Cornejo, J. A.; Sheng, H.; Edri, E. Ajo-Franklin, C. A.; Frei, H. Nanoscale Membranes that Chemically Isolate and Electronically Wire up the Abiotic/Biotic Interface. *Nature Commun.* **2018**, *9*, article no 2263.

[16] Katsoukis, G.; Jo, W. J.; Frei, H. Structure and Orientation of Molecular Wires Embedded in Ultrathin Silica Membrane for Artificial Photosynthesis Elucidated by Polarized FT-IRRAS. *J. Phys. Chem. C* **2019**, *123*, 18905-18913.

[17] Katsoukis, G.; Frei, H. Ultrathin Oxide Layers for Nanoscale Integration of Molecular Light Absorbers, Catalysts, and Complete Artificial Photosystems. *J. Chem. Phys.* **2019**, *150*, article no 041501.

[18] Jo, W. J.; Katsoukis, G.; Frei, H. Ultrathin Amorphous Silica Membrane Enhances Proton Transfer across Solid-to-Solid Interfaces of Stacked Metal Oxide Nanolayers while Blocking Oxygen. *Adv. Funct. Mater.* **2020**, *30*, article no 1909262.

[19] Shimidzu, T.; Iyoda, T.; Izaki, K. Photoelectrochemical Properties of Bis(2,2'-bipyridine) (4,4'-dicarboxy-2,2'-bipyridine)ruthenium(II) Chloride. *J. Phys. Chem.* **1985**, *89*, 642-645.

[20] Kolb, H. C.; Finn, M. G.; Sharpless, K. B. Click Chemistry: Diverse Chemical Function from a Few Good Reactions. *Angew. Chem. Int. Ed.* **2001**, *40*, 2004-2021.

[21] Kellner, S. Charge Transport via Molecular Wires Embedded in an Ultrathin Planar Insulating Membrane. *Master Thesis*, University of Erlangen-Nuernberg, 2019.

[22] Yuan, G.; Agiral, A.; Pellet, N.; Kim, W.; Frei, H. Inorganic Core-Shell Assemblies for Closing the Artificial Photosynthetic Cycle. *Faraday Discuss.* **2014**, *176*, 233-249.

[23] Zhang, M.; de Respinis, M.; Frei, H. Time-Resolved Observations of Water Oxidation Intermediates on a Cobalt Oxide Nanoparticle Catalyst. *Nature Chem.* **2014**, *6*, 362-367.

[24] Brautigam, M.; Kubel, J.; Schulz, M.; Vos, J. G.; Dietzek, B. Hole Injection Dynamics form two Structurally Related Ru-bipyridine complexes into NiO_x is determined by the substitution pattern of the ligands. *Phys. Chem. Chem. Phys.* **2015**, *17*, 7823-7830.

[25] Azam, M. S.; Fenwick, S. L.; Gibbs-Davis, J. M. Orthogonally Reactive SAMs as a General Platform for Bifunctional Silica Surfaces. *Langmuir* **2011**, *27*, 741-750.

[26] Hollins, P. In *Encyclopedia of Analytical Chemistry;* Meyers, R. A., Ed.; Wiley: New York, 2006; p. 1.

[27] Billes, F.; Endredi, H.; Keresztury, G. Vibrational Spectroscopy of Triazoles and Tetrazole. *J. Mol. Struct.* **2000**, *530*, 183-200.

[28] Colthup, N. B.; Daly, L. H.; Wiberley, S. E. *Introduction to Infrared and Raman Spectroscopy;* Academic Press: London, 1990; p. 374–380.

[29] Bellamy, L. J. *The Infrared Spectra of Complex Molecules;* Chapman and Hall: London, 1975; Vol. 1, p. 395.

[30] Lukes, V.; Polovkova, J.; Rapta, P.; Vegh, D. The Experimental and Theoretical Characterization of the Phenyl-perfluorophenyl π-π and Hydrogen Bond Interactions in the Aldimine Co-crystal. *Chem. Phys.* **2006**, *326*, 271-280.

[31] Colthup, N. B.; Daly, L. H.; Wiberley, S. E. *Introduction to Infrared and Raman Spectroscopy;* Academic Press: London, 1990; p. 221.

[32] Bellamy, L. J. *The Infrared Spectra of Complex Molecules;* Chapman and Hall: London, 1975; Vol. 1, p. 132.

[33] Colthup, N. B.; Daly, L. H.; Wiberley, S. E. *Introduction to Infrared and Raman Spectroscopy;* Academic Press: London, 1990; p. 328.

[34] Swierk, J. R.; McCool, N. S.; Nemes, C. T.; Mallouk, T. E. Schmuttenmaer, C. A. Ultrafast Electron Injection Dynamics of Photoanodes for Water Splitting Dye Sensitized Photoelectrochemical Cells. *J. Phys. Chem. C* **2016**, *120*, 5940-5948.

[35] Shimidzu, T.; Iyoda, T.; Izaki, K. Photoelectrochemical Properties of Bis(2,2'-bipyridine) (4,4'-dicarboxy-2,2'-bipyridine)ruthenium(II) Chloride. *J. Phys. Chem.* **1985**, *89*, 642-645.

[36] Song, W.; Brennaman, M. K.; Concepcion, J. J.; Jurss, J. W.; Hoertz, P. G.; Luo, H.; Chen, C.; Hanson, K.; Meyer, T. J. Interfacial Electron Transfer Dynamics for $[Ru(bpy)_2((4,4'\text{-}PO_3H)_2bpy)]^{2+}$ Sensitized TiO_2 in a Dye-Sensitized Photoelectrosynthesis Cell: Factors Influencing Efficiency and Dynamics. *J. Phys. Chem. C* **2011**, *115*, 7081-7091.

[37] Lee, S. H. A.; Zhao, Y.; Hernandez-Pagan, E. A.; Blasdel, L.; Youngblood, J.; Mallouk, T. E. Electron Transfer Kinetics in Water Splitting Dye-Sensitized Solar Cells Based on Core-Shell Oxide Electrodes. *Faraday Discuss.* **2012**, *155*, 165-176.

[38] Perez-Leon, C; Kador, L.; Peng, B.; Thelakkat, M. Characterization of the Absorption of Ru-bpy Dyes on Mesoporous TiO_2 Films with UV-Vis, Raman, and FT-IR Spectroscopies. *J. Phys. Chem. B* **2006**, *110*, 8723-8730.

[39] Soo, H. S.; Agiral, A.; Bachmeier, A.; Frei, H. Visible Light-Induced Hole Injection into Rectifying Molecular Wires Anchored on Co_3O_4 and SiO_2 Nanoparticles. *J. Am. Chem. Soc.* **2012**, *134*, 17104-17116.

[40] Son, H. J.; Wang, X.; Prasittichai, C.; Jeong, N. C.; Aaltonen, T.; Gordon, R. G.; Hupp, J. T. Glass-Encapsulated Light Harvesters: More Efficient Dye-Sensitized Solar Cells by

Deposition of Self-Aligned, Conformal, and Self-Limited Layers. *J. Am. Chem. Soc.* **2012**, *134*, 9537-9540.

[41] Marcus, R. A.; Sutin, N. Electron Transfer in Chemistry and Biology. *Biochim. Biophys. Acta* **1985**, *811*, 265-322.

[42] Ding, W.; Negre, C. F. A.; Palma, J. L.; Durrell, A. C.; Allen, L. J.; Young, K. J.; Milot, R. L.; Schmuttenmaer, C. A.; Brudvig, G. W.; Crabtree, R. H.; Batista, V. S. Linker Rectifiers for Covalent Attachment of Transition Metal Catalysts to Metal-Oxide Surfaces. *ChemPhysChem* **2014**, *15*, 1138-1147.

[43] Chitre, K.; Batarseh, A.; Kopecky, A.; Fan, H.; Tang, H.; Lalancette, R.; Bartynski, R. A.; Galoppini, E. Synthesis of Zinc Tetraphenylporphyrin Rigid Rods with a Built-in Dipole. *J. Phys. Chem. B* **2015**, *119*, 7522-7530.

[44] Ngo, K. T.; Rochford, J.; Fan, H.; Batarseh, A.; Chitre, K.; Rangan, S.; Bartynski, R. A.; Galoppini, E. Photoelectrochemical Properties of Porphyrin Dyes with a Molecular Dipole in the Linker. *Faraday Discuss.* **2015**, *185*, 497-506.

[45] Rangan, S.; Batarseh, A.; Chitre, K. P.; Kopecky, A.; Galoppini, E.; Bartynski, R. A. Tuning Energy Level Alignment at Organic/Semiconductor Interfaces Using a Built-in Dipole in Chromophore-Bridge-Anchor Compounds. *J. Phys. Chem. C* **2014**, *116*, 12923-12928.

[46] Nieto-Pescador, J.; Abraham, B.; Li, J.; Batarseh, A.; Bartynski, R. A.; Galoppini, E.; Gundlach, L. Heterogeneous Electron Transfer Dynamics through Dipole-Bridge Groups. *J. Phys. Chem. C* **2016**, *120*, 48-55.

[47] De Miguel, G.; Wielopolski, M.; Schuster, D. I.; Fazio, M. A.; Lee, O. P.; Haley, C. K.; Ortiz, A. L.; Echegoyen, L.; Clark, T.; Guldi, D. M. Triazole Bridges as Versatile Linkers in Electron Donor-Acceptor Conjugates. *J. Am. Chem. Soc.* **2011**, *133*, 13036-13054.

Table 1: FT-IRRAS of TMSBA attached on Co_3O_4 (trace (1)) and click attached wire molecules (trace (2) of Figures 3, 4, and 5) (ν = stretch, δ = in-plane bend, β = in-plane ring bend, γ = out-of-plane ring bend).

TMSBA	E-PV3-SO_3Et	E-PV3-OMe	E-PV3-F_5	Assignment
2100				$\nu_{as}(N_3)$
1600				ν_{aryl}
	1590	1588	1588	ν_{aryl}
1549				ν_{aryl}
	1520	1513	1520	ν_{aryl} (admixed ν(C-F))
1497				ν_{aryl}
			1491	ν_{aryl}, ν(C-F)
		1456		$\delta_{as}(CH_3)$
1449				$\delta_{as}(CH_2)$
1400				ν_{aryl}
	1369			$\delta_{sym}(CH_3)$
	1343			$\nu_{as}(SO_2)$
	1308	1302		
		1253		$\nu(C_{aryl}\text{-O-C})$
			1217	ν_{ring}(Tz)
	1188			$\nu_{sym}(SO_2)$
1181				δ_{aryl}(CCH)
	1167	1173	1156	ν_{ring}(Tz) (admixed $\nu_{sym}(SO_2)$)
1129				$\nu(Si(OCo)_3)$
1100				$\nu(Si(OCo)_3)$
1021				$\nu(Si(OCo)_3)$
			1002	ν(C-F)
	998			δ(C=C-C), ν(C-C), ν(C-S)

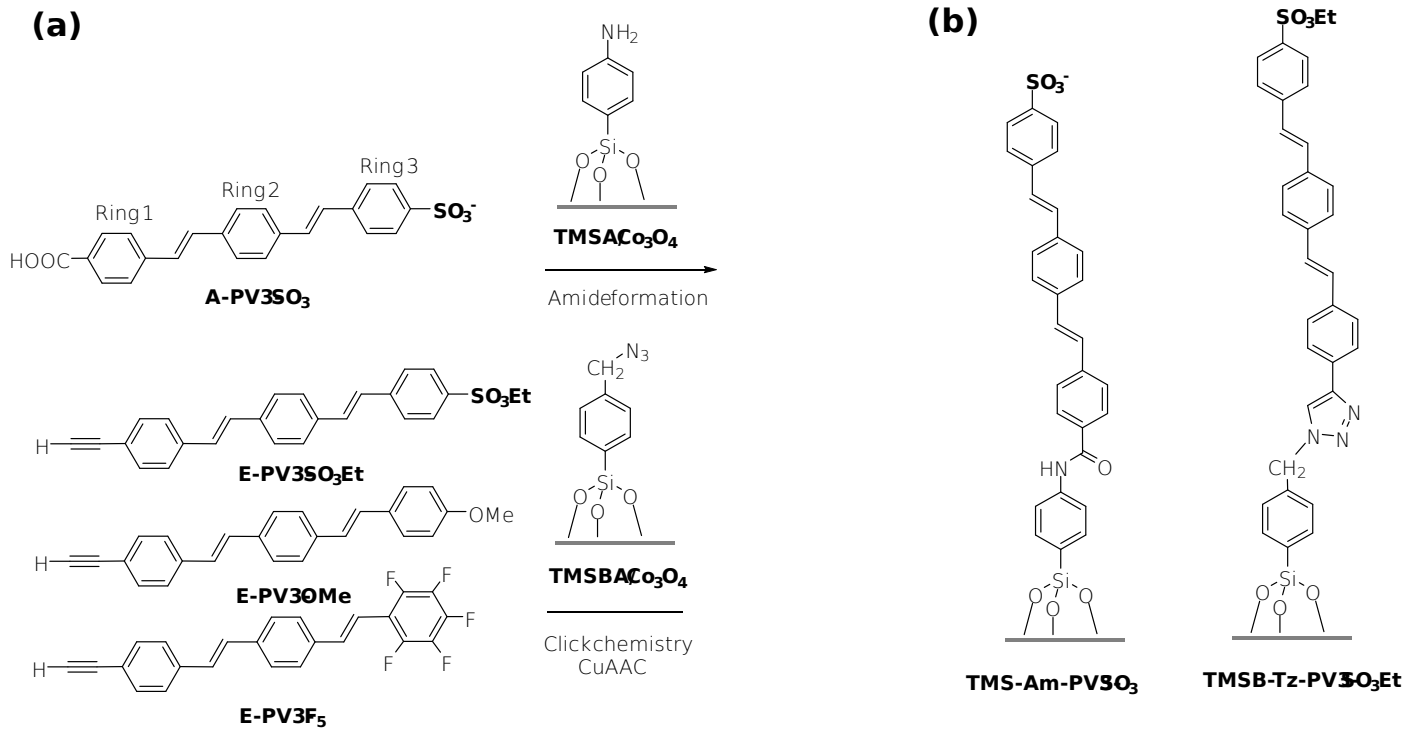

Scheme 1: (a) Functionalized wire molecules with electron donating and withdrawing groups. A-PV3-SO_3: -6.43 eV (1.93 V), 1.48 V; E-PV3-SO_3Et: -6.11 eV (1.61 V), 1.16 V; E-PV3-F_5: -6.18 eV (1.68 V), 1.23 V; E-PV3-OMe: -5.59 eV (1.09 V), 0.64 V. The first value is the HOMO potential of the free wire calculated by DFT (vacuum), followed in parenthesis in V vs. NHE. The last value is the potential of the wire linked to the anchor (vs. NHE). A-PV3 and E-PV3 designate wire functionalized on ring 1 by acid or ethyne group for amide (Am) of triazole (Tz) attachment to anchor, respectively. **(b)** Wires attached to anchor molecules: TMS-Am-PV3-SO_3: -5.98 eV (1.48 V vs. NHE); TMSB-Tz-PV3-SO_3Et: -5.66 eV (1.16 V vs. NHE).

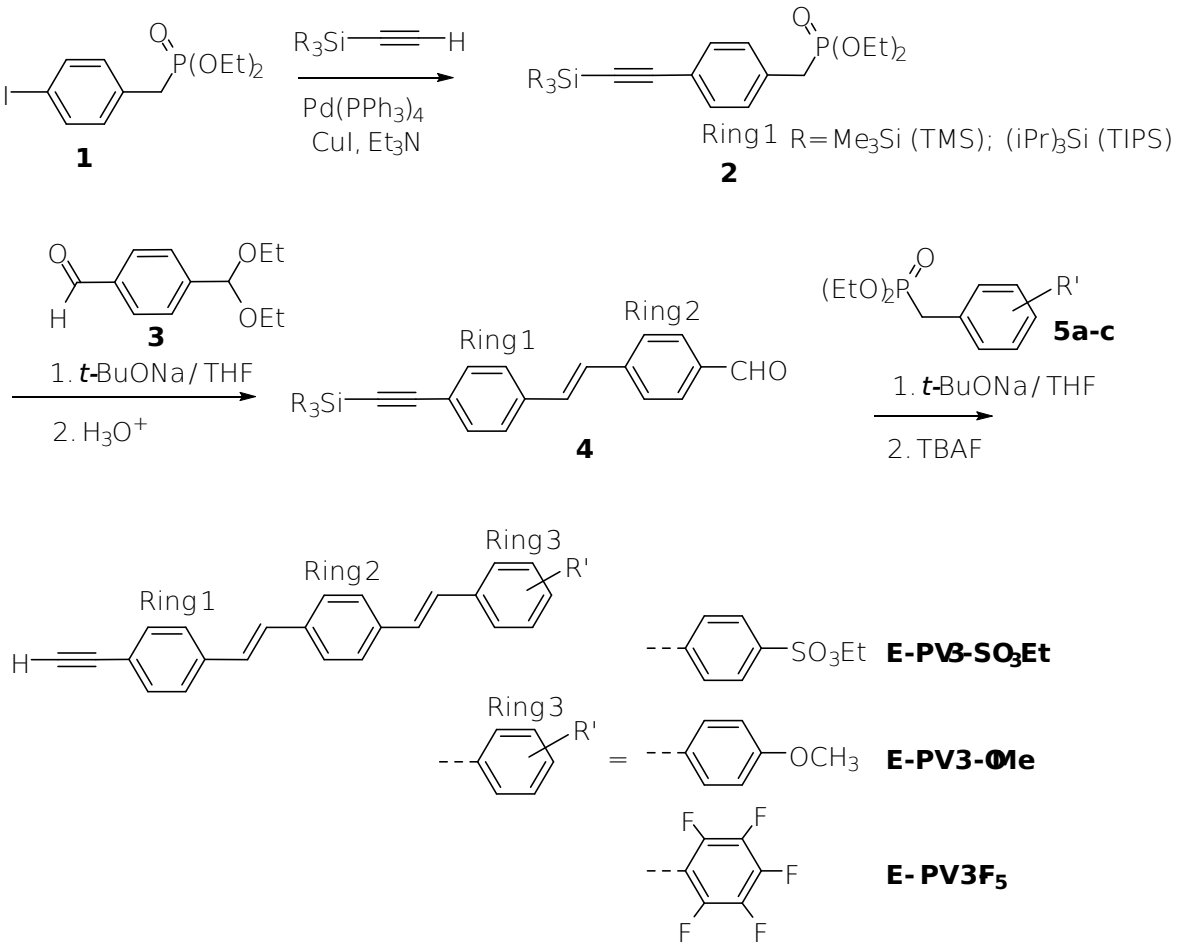

Scheme 2. Synthesis of click-ready molecular wires modified by electron withdrawing and donating substituents on ring 3.

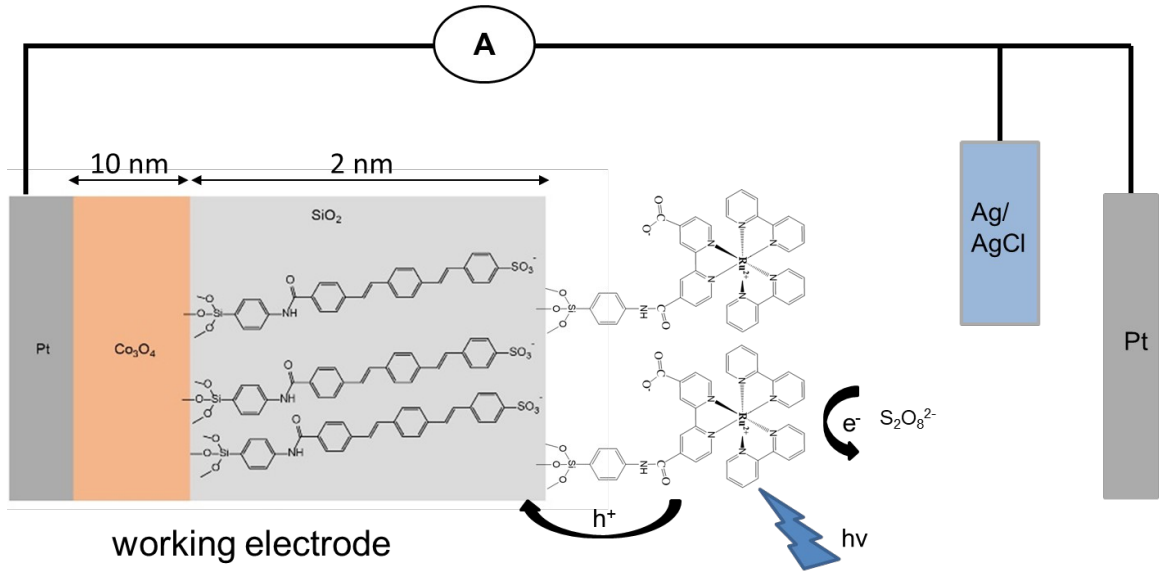

Figure 1: Schematic of ultrathin silica membrane with embedded molecular wires and covalently light absorbers covalently (but randomly) anchored on the silica surface. The samples deposited on Pt are the working electrode for photocurrent measurements in a 3-electrode cell. Pt wires and Ag/AgCl were used as counter and reference electrodes, respectively.

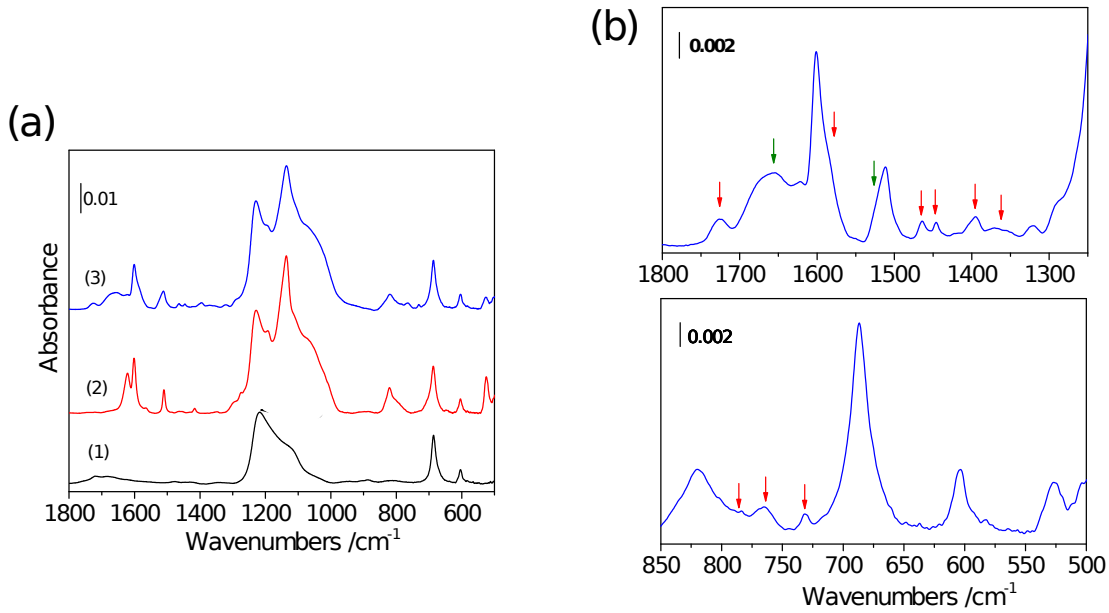

Figure 2: FT-IRRAS of $[Ru(bpy)_2(dcbpy)]^{2+}$ light absorber attached by TMSA on silica of Pt/ Co_3O_4 (10 nm)/SiO_2 (2 nm) sample. **(a)** Trace (1): Pt/Co_3O_4 (10 nm)/SiO_2 (2 nm). Trace (2): After attachment of TMSA anchor. Trace (3): After attachment of $[Ru(bpy)_2(dcbpy)]^{2+}$ to TMSA anchor by amide bond. **(b)** Expanded spectrum (3) 1800-1250 cm^{-1} and 850-500 cm^{-1}, red arrows indicate $[Ru(bpy)_2(dcbpy)]^{2+}$ bands, green arrows are modes of amide linkage.

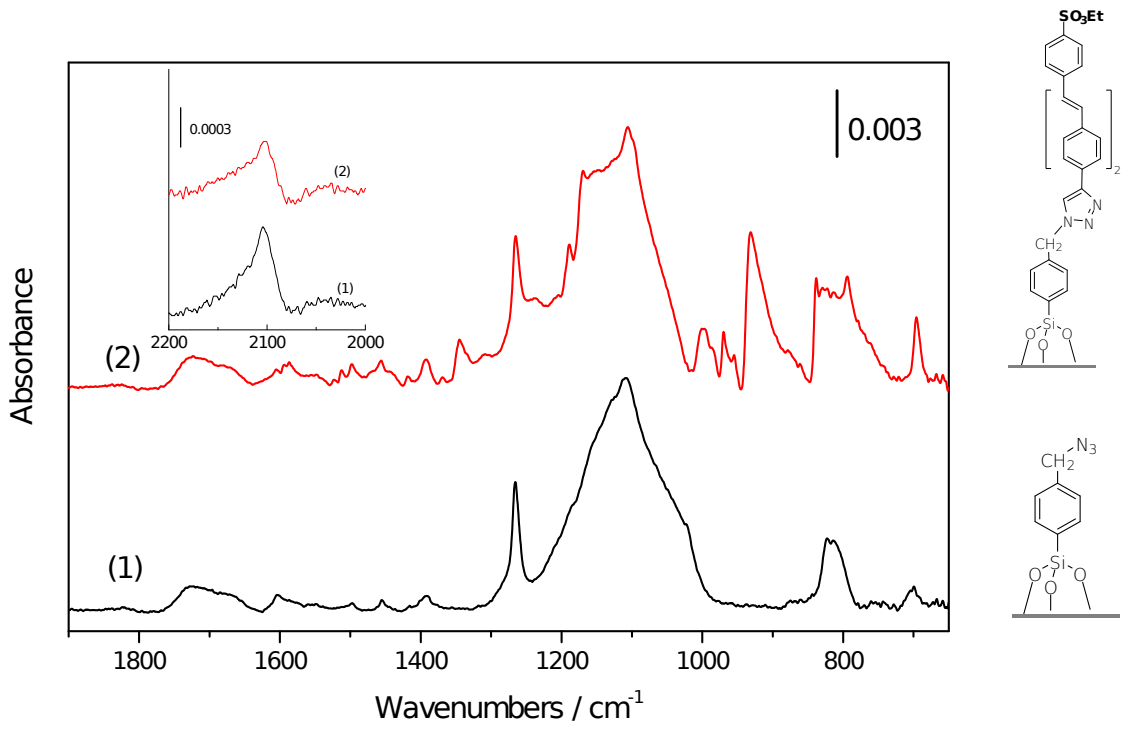

Figure 3: FT-IRRAS of E-PV3-SO_3Et wire attachment by click chemistry to TMSBA anchor on Co_3O_4. Trace (1): TMSBA anchored on Co_3O_4. Trace (2): After attachment of E-PV3-SO_3Et to anchor. Inset: Expanded $\nu_{as}(N_3)$ region shows band before (black) and after E-PV3-SO_3Et attachment by click reaction (red). Broad absorption 1620-1760 cm^{-1} is due to oxide background, and sharp band at 1263 cm^{-1} due to residual Pt background.

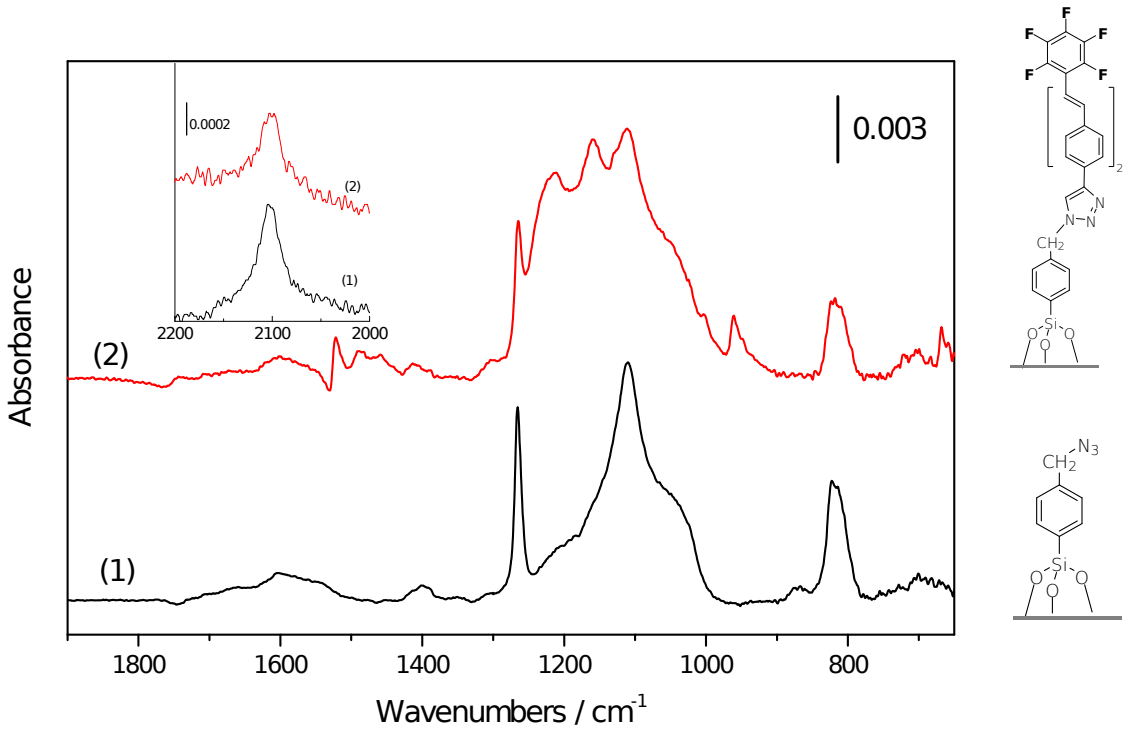

Figure 4: FT-IRRAS of E-PV3-F_5 wire attachment by click chemistry to TMSBA anchor on Co_3O_4. Trace (1): TMSBA anchored on Co_3O_4. Trace (2): After click reaction of E-PV3-F_5 with anchor. Inset: Expanded $\nu_{as}(N_3)$ region shows band before and after E-PV3-F_5 attachment. Sharp band at 1263 cm^{-1} is due to residual Pt background.

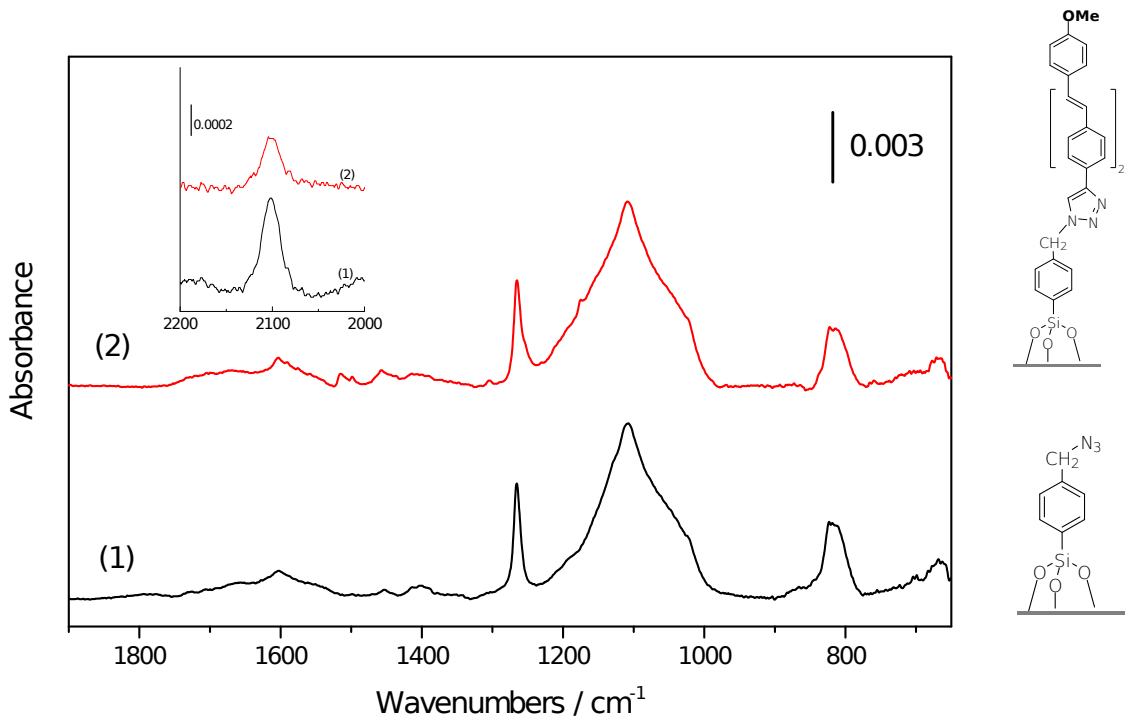

Figure 5: FT-IRRAS of E-PV3-OMe wire attachment by click chemistry to TMSBA anchor on Co_3O_4. Trace (1): TMSBA anchored on Co_3O_4. Trace (2): After attachment of E-PV3-OMe to TMSBA anchor. Inset: Expanded $\nu_{as}(N_3)$ NNN stretch region shows band before and after E-PV3-OMe attachment. Sharp band at 1263 cm^{-1} is due to residual Pt background.

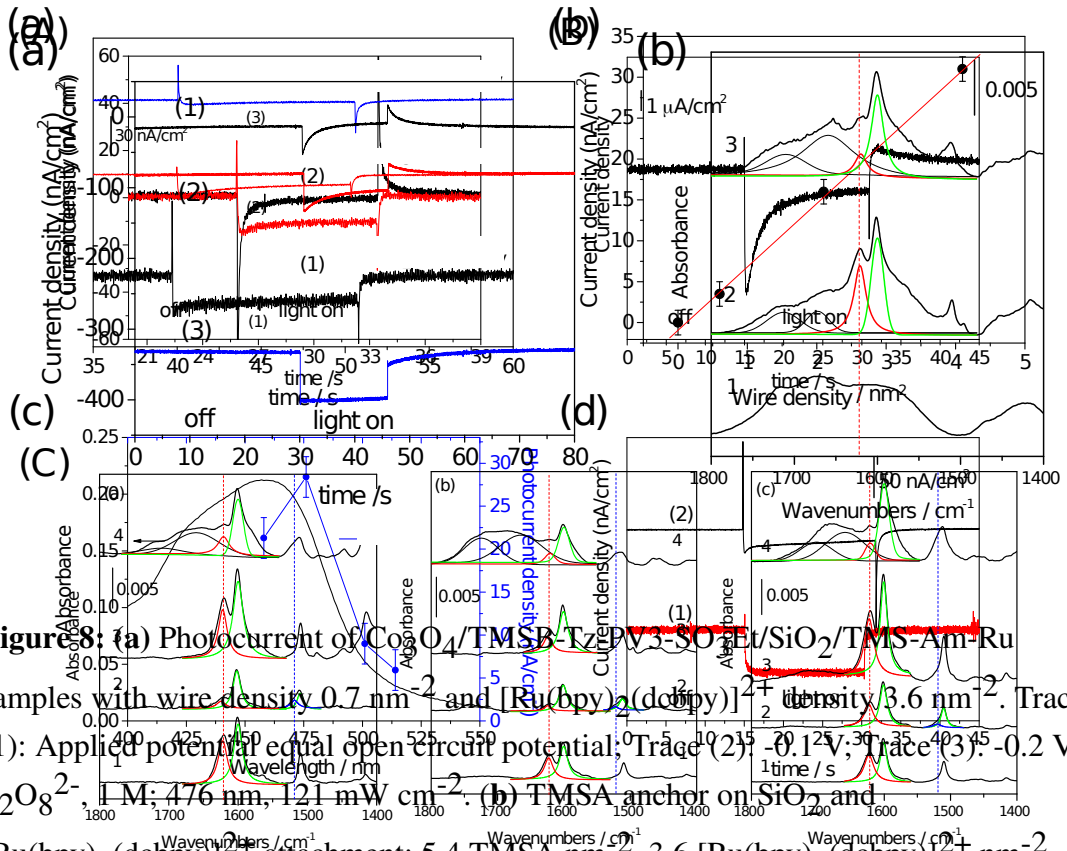

Figure 8: (**a**) Photocurrent of Co_3O_4/TMSB-Tz-PV3-SO_3Et/SiO_2/TMS-Am-Ru samples with wire density 0.7 nm^{-2} and $[Ru(bpy)_2(dcbpy)]^{2+}$ density 3.6 nm^{-2}. Trace (1): Applied potential equal open circuit potential; Trace (2): -0.1 V; Trace (3): -0.2 V. $S_2O_8^{2-}$, 1 M; 476 nm, 121 mW cm^{-2}. (**b**) TMSA anchor on SiO_2 and $[Ru(bpy)_2(dcbpy)]^{2+}$ attachment: 5.4 TMSA nm^{-2}, 3.6 $[Ru(bpy)_2(dcbpy)]^{2+}$ nm^{-2}.

Figure 6: Photocurrent upon 476 nm illumination (121 mW cm^{-2}). (**a**) Trace (1): Trace (1): Pt/Co_3O_4/TMSB-Tz-PV3-SO_3Et/SiO_2. Trace (2): After anchoring of TMSA. Pt/Co_3O_4/TMS-Am-PV3-SO_3/SiO_2/TMS-Am-Ru. Trace (2): Pt/Co_3O_4/SiO_2/TMS-Am-Ru (no wires in membrane). (**b**) Photocurrent of Pt/Co_3O_4/TMS-Am-PV3-SO_3/SiO_2/TMS-Am-Ru/TiO_2 sample upon 476 nm illumination (2.580 mW cm^{-2}). 3.2A-PV3-SO_3 samples with wire density (1) 4.1 nm^{-2}, (2) 2.1 nm^{-2}, (3) 0.6 nm^{-2}. $S_2O_8^{2-}$, 1 M; 476 nm, 121 mW cm^{-2}. (**B**) Wire density dependence of photocurrent. (**C**) FT-IRRAS for determining wire and light absorber density of each sample. (a) 4.1 A-PV3-SO_3 nm^{-2}, 2.8 Ru nm^{-2}; (b) 2.1 A-PV3-SO_3 nm^{-2}, 1.0 Ru nm^{-2}; (c) 0.6 A-PV3-SO_3 nm^{-2}, 3.7 Ru nm^{-2}. (1) Co_3O_4/TMSA; (2) Co_3O_4/TMS-Am-PV3-SO_3; (3) Co_3O_4/TMS-Am-PV3-SO_3/SiO_2/TMSA; (4) Co_3O_4/TMS-Am-PV3-SO_3/SiO_2/TMS-Am-Ru.

Figure 7: (**A**) Photocurrent of Co_3O_4/TMS-Am-PV3-SO_3/SiO_2/TMS-Am-Ru samples with wire density (1) 4.1 nm^{-2}, (2) 2.1 nm^{-2}, (3) 0.6 nm^{-2}. $S_2O_8^{2-}$, 1 M; 476 nm, 121 mW cm^{-2}. (**B**) Left Y-scale: Absorbance of $[Ru(bpy)_2(dcbpy)]^{2+}$ (spectrum recorded in aqueous solution). Right Y-scale: Photocurrent density. The red shift of the photocurrent excitation spectrum relative to the absorption band of the Ru complex in solution is in agreement with red shifts for Ru complexes attached to TiO_2 reported in the literature. [37b] The photocurrent value at 458 nm is within uncertainty in agreement with the absorption profile. (**d**) Trace (1): Photocurrent for Pt/Co_3O_4/TMS-Am-Ru sample (no silica membrane), Ru density 5.8 nm^{-2}. Trace (2): Photocurrent of Pt/Co_3O_4/TMS-Am-PV3-SO_3/SiO_2/TMS-Am-Ru sample, A-PV3-SO_3 density 6.0 nm^{-2}, Ru density 8.8 nm^{-2}.

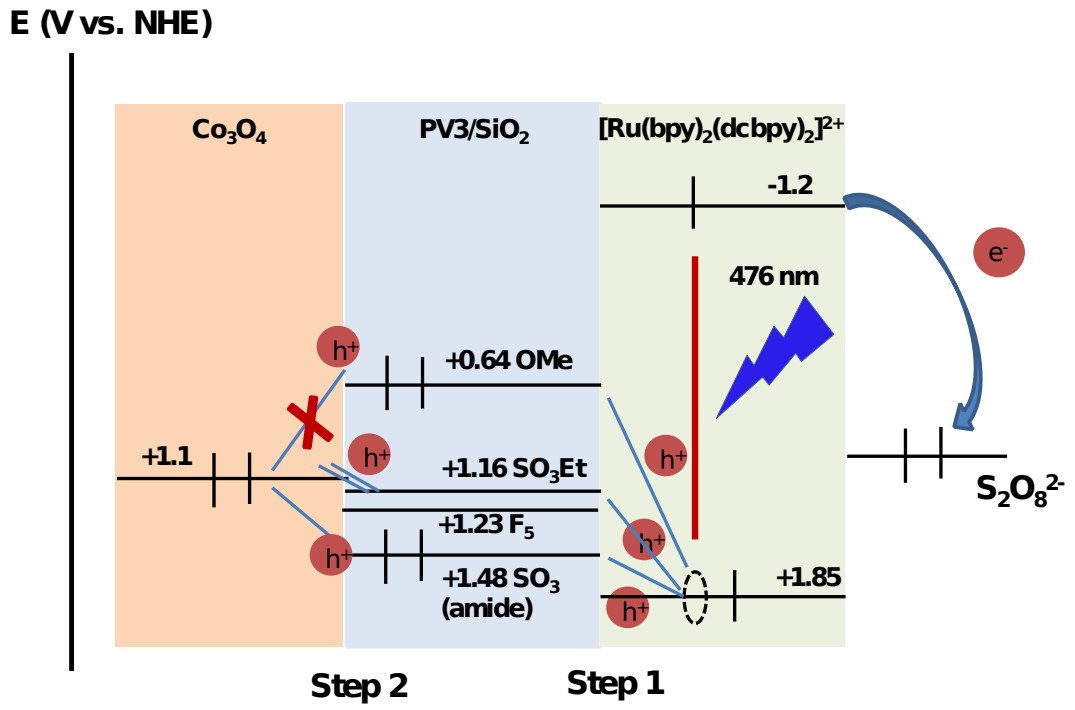

Figure 9: Energy level alignment of HOMO of molecular wires with HOMO of $[Ru((bpy)_2(dcbpy)]^{2+}$ light absorber and Co_3O_4 catalyst valence band. In the scheme, anchored wires are abbreviated as OMe for E-PV3-OMe, SO_3Et for E-PV3-SO_3Et, F_5 for E-PV3-F_5, and SO_3 for A-PV3-SO_3.

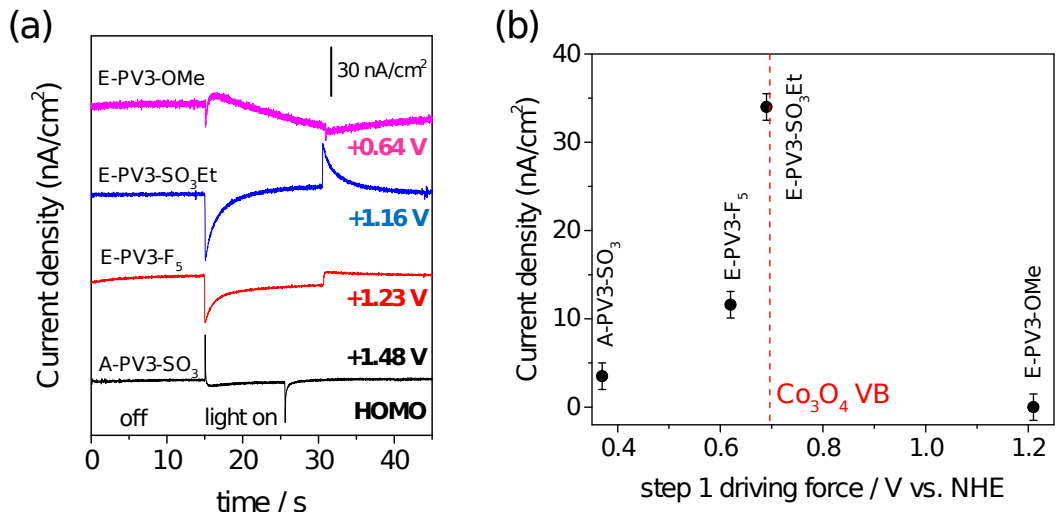

Figure 10: (a) Photocurrent of Co_3O_4/wire/SiO_2/TMS-Am-Ru at OCP for different embedded wires. Top to bottom: E-PV3-OMe (0.5 nm^{-2}), 1.2 Ru nm^{-2}. E-PV3-SO_3Et (0.7 nm^{-2}), 3.6 Ru nm^{-2} (from Figure 8(a) trace (1)). E-PV3-F_5 (1.46 nm^{-2}), 6.5 Ru nm^{-2}. A-PV3-SO_3 (0.6 nm^{-2}), 3.7 Ru nm^{-2} (from Figure 7A trace (3)). **(b)** Photocurrent dependence on HOMO potential of embedded wire molecule, normalized for wire density of 0.6 nm^{-2}.

TOC graphics